[American Journal of Science, Vol. 319, February, 2019, P. 122–157, DOI 10.2475/02.2019.03]

SHALLOW WATER REDOX CONDITIONS OF THE MID-PROTEROZOIC MUSKWA ASSEMBLAGE, BRITISH COLUMBIA, CANADA

ERIC J. BELLEFROID*,†, NOAH J. PLANAVSKY*,†, ASHLEIGH V. S. HOOD*, GALEN P. HALVERSON**, and KASPARAS SPOKAS**,***

ABSTRACT. The mid-Proterozoic was a time of apparent prolonged biological and geochemical stability, preceeding the environmental turmoil and rapid biological innovations that characterized the Neoproterozoic. Despite an upswing in work on the mid-Proterozoic over the past decade, basic aspects of the carbon cycle and Earth's surface redox state during this time period remain poorly understood. To provide a new window into the mid-Proterozoic environmental evolution, we have investigated carbonates in the well-exposed Muskwa Assemblage located in NE British Columbia, Canada, for a combined stratigraphic and geochemical study. Rare Earth Elements and Yttrium (REE+Y) geochemistry was applied to carbonate rocks deposited over a marine paleoenvironmental depth gradient in order to characterize prevailing water column redox conditions. These data provide evidence for an extremely shallow chemocline with oxic surface waters being restricted to within storm-wave base, which is consistent with globally low oxygen in the ocean-atmosphere system. Furthermore, there is evidence for facies-dependent carbonate $\delta^{13}C$ variability within the Muskwa Assemblage comparable in scale to typical stratigraphic variability recorded in carbonate strata of this age, highlighting the problems of using small carbon isotope excursions for chemostratigraphy.

Keywords: Rare Earth Element, carbonate, Ce anomaly, carbon isotope, Mesoproterozoic, Paleoproterozoic

INTRODUCTION

The mid-Proterozoic (the late Paleoproterozoic to the early Neoproterozoic, 1.8 Ga – 0.8 Ga) is a time period characterized by biogeochemical, climatic, and evolutionary stasis. Exemplary of this period's environmental stability, there has been limited evidence for continental ice sheets, suggesting climatic stability (Planavsky and others, 2015), and muted variation in the carbon isotope compositions ($\delta^{13}C$) of marine carbonates and organic carbon suggesting global carbon cycle stasis (Braiser and Lindsay, 1998; Kah and others, 1999; Bartley and Kah, 2004). Although this period hosted some major evolutionary events, such as the emergence of eukaryotes (Lamb and others, 2009; Peng and others, 2009) and algae (Butterfield, 2000), diversification rates remained sluggish in comparison to the later Proterozoic and Phanerozoic (Knoll, 2014) and eukaryotic contribution to the biosphere was limited. As a consequence of this apparent environmental stability, this time interval has been referred to as "the most boring billion years of Earth's history" (Braiser and Lindsay, 1998; Holland, 2006), or more simply, 'the boring billion'. This apparent stability contrasts strongly with the preceeding late Neoproterozoic (0.8 – 0.54 Ga), which was characterized by extreme biological, geochemical, and climatic volatility (for example Kah and others, 1999; Halverson and others, 2007; Tosca and others, 2010; Knoll 2014), including low-latitude Cryogenian ice ages and associated negative $\delta^{13}C$ anomalies (Hoffman and others, 1998; Evans, 2003). Neoproterozoic shallow marine environments also set the stage

* Department of Geology and Geophysics, Yale University, 210 Whitney Avenue, New Haven, Connecticut, USA 06511
** Department of Earth and Planetary Sciences, McGill University, 3450 University Street, Montreal, Quebec, Canada H3A 0E8
*** Department of Civil and Environmental Engineering, Princeton University, E-208 E-Quad, Princeton, New Jersey, USA 08544
† Corresponding authors: Tel: 1-203-589-2304, E-mail: eric.bellefroid@yale.edu; noah.planavsky@yale.edu

for the emergence of animals (for example Wood and others, 2015), and eukaryotes, which likely began to play a critical role in shaping ecosystems at this time (Butterfield, 2011; Brocks and others, 2017). Although the Neoproterozoic marks a crucial shift in global biogeochemical cycling, understanding the feedbacks and environmental conditions that allowed for the preceding 'boring billion' is essential to deciphering the factors that drove these late Neoproterozoic revolutions.

Ocean and atmospheric oxygen levels were significantly lower in the mid-Proterozoic than in the late Neoproterozoic and Phanerozoic, and increasing oxygen concentrations is one of the factors thought to mark the end of the boring billion (Planavsky and others, 2015; Reinhard and others, 2016). Although there may have been some intervals or basins during the mid-Proterozoic with suboxic (Slack and others, 2007; Bekker and others, 2014) and or even fully oxic deep-waters (for example Sperling and others, 2014), these may reflect temporal and spatial heterogeneity in marine oxygen levels. The overarching consensus is that the deep-ocean remained largely anoxic, even as the surface ocean was at least mildly oxygenated (Canfield and others, 2008; Poulton and Canfield, 2011; Lyons and others, 2014; Reinhard and others, 2016). In contrast, estimates of mid-Proterozoic surface water oxygen levels and atmospheric oxygen partial pressures (pO_2) are arguably weaker. Based on the scarcity of detrital pyrite and the acceptance of generally anoxic deep oceans (Kump, 2008), initial estimates of mid-Proterozoic atmospheric oxygen levels were between ~1 and 40 percent of present atmospheric levels (PAL). Evidence of iron loss from some well-preserved mid-Proterozoic paleosols suggest pO_2 levels less than ~1 percent PAL (Pinto and Holland, 1988; Mitchel and Sheldon, 2009). More recent work using Cr isotopes in black shales and ironstones, which indicate when atmospheric oxygen concentrations in the atmosphere were high enough to fractionate chromium isotopes during subaerial weathering, estimate a much narrower range between < 0.1 percent to <1 percent PAL during the mid-Proterozoic (Crowe and others, 2013; Planavsky and others, 2014; Cole and others, 2016, compare with Gilleaudeau and others, 2016; Canfield and others, 2018). However, precise estimates of the atmospheric oxygen levels needed to induce Cr oxidation and subsequent preservation of large Cr isotope fractionations in marine sediments are still being refined (for example Wang and others, 2015; D'Arcy and others, 2016). This uncertainty allows that mid-Proterozoic atmospheric oxygen concentrations likely varied. Regardless, if baseline atmospheric oxygen levels were <1 percent PAL throughout the Proterozoic, the oceans would have been a hostile place for animals and possibly even single-celled eukaryotes, placing a break on eukaryote diversification (Reinhard and others, 2016).

Although the marine redox landscape is controlled in part by the strength of the biological pump, low atmospheric pO_2 levels would be expressed as a shallow chemocline in portions of the oceans (Olson and others, 2013; Reinhard and others, 2016), providing a means to test the new idea of sustained low atmospheric oxygen levels in the mid-Proterozoic using geochemical techniques on shallow marine lithologies. We present new work geared towards improving our understanding of mid-Proterozoic redox evolution and carbon cycling. We have targeted shallow marine carbonates, which precipitate from seawater over recognizable depth ranges and can provide a more direct record of shallow seawater chemistry (for example Hotinski and others, 2004; Hood and Wallace, 2014, 2015). Specifically, we have undertaken a combined stratigraphic-geochemical study of the Mid-Proterozoic Muskwa Assemblage, a well-exposed, and dominantly carbonate sequence that presents an obvious target for paleoredox work (Bell, 1968). We focus on REE+Y data, in particular, Ce anomalies since they are well-characterized in modern environments (Elderfield and Sholkovitz, 1987; German and Elderfield, 1990; German and others, 1991; Bau and others, 1997; Bau, 1999; Haley and others, 2004; Bau and Koschinsky, 2009; Planavsky and others,

2010), and in contrast to many carbonate archives, have been demonstrated in multiple studies to preserve primary seawater values (Banner and others, 1988b; Sholkovitz and Shen, 1995; Nothdurft and others, 2004; Bau and Alexander, 2006; Wallace and others, 2017; Hood and others, 2018; Liu and others, 2019). In particular, the abundance of Ce relative to other REE+Y in marine carbonates may be used as a proxy for the redox state of the parent seawater during carbonate precipitation, because Ce is redox-sensitive (Bau and others, 1996; Bau and Koschinsky, 2009). Using sedimentary facies assignments to constrain paleo-depth, we measured REE+Y (Rare Earth Elements and Yttrium) and $\delta^{13}C$ to determine the redox conditions of the water column, and the magnitude of the $\delta^{13}C$ gradient across the basin.

GEOLOGICAL SETTING

The Proterozoic Muskwa Assemblage is a ~6 km thick, mixed carbonate and siliciclastic succession located in the Rocky Mountains of northeastern British Columbia, Canada (Bell, ms, 1966, 1968; Taylor and Stott, 1973). Situated 200 km west of Fort Nelson, the succession is exposed in a large, west-plunging asymmetric anticline, with a series of east-verging thrust faults and west-dipping normal faults truncating sections (Bell, ms 1966, 1968; Taylor and Stott, 1973; Thompson, 1981). The lower part of the Muskwa Assemblage outcrops within the core of the anticline, whereas thrusted and normal faulted blocks on the western limb of the fold expose the upper part of the succession (fig. 1). The lower Muskwa Assemblage records deposition on a carbonate ramp, seaward of a large western-draining delta, sourcing clastic sediment from the Canadian Shield (Bell, ms 1966, 1968; Ross and others, 2001; Cook and others, 2004). Broad-scale E-W seismic profiles suggest a thick and laterally extensive Mid-Proterozoic sedimentary unit at depth, which is interpreted to be a continuation of the exposed Muskwa Assemblage (Cook and others, 2004). The sequence is interpreted to have been deposited upon Paleoproterozoic granite basement (Villeneuve and others, 1991; Cook and Van der Velden, 1993). While exposed strata are measured to be 6 km thick, total thickness, including unexposed strata, is inferred to be between 7 to 20 km, depending on seismic interpretations (Long and others, 1999; Cook and others, 2004; Evenchick and others, 2005).

The Assemblage is separated into seven lithostratigraphic units (fig. 2). The lower four formations, the Chischa Formation (Fm.), the Tetsa Fm., the George Fm. and the Henry Creek Fm., are dominated by mixed fine-grained siliciclastics and carbonates (Bell, ms 1966, 1968; Taylor and Stott, 1973). The upper three formations, the Tuchodi Fm., the Aida Fm. and the Gataga Fm., are dominantly siliciclastic, except parts of the lower and middle Tuchodi Fm., which are carbonate (Bell, ms 1966, 1968; Taylor and Stott, 1973). It is important to note that the latter of the three, the Gataga Fm., is not to be confused with Cryogenian aged units exposed to the west of Tuchodi lakes area in the Gataga Mountain area bearing a similar name (Ferri and others, 1999). The Muskwa Assemblage is unconformably overlain by the early Cambrian Atan Group, which comprises a series of alluvial fan conglomerates deposited adjacent to active faults (Taylor and Stott, 1973). Both Proterozoic and overlying Phanerozoic sedimentary units were deformed during thin-skin Laramide thrusting (Taylor and Stott, 1973; Thompson, 1981). Though deformed, the Muskwa Assemblage has experienced only low grade (sub-greenschist grade facies) metamorphism (Bell, ms 1966, 1968; Taylor and Stott, 1973) with little obvious late-stage fluid flow.

Absolute age constraints for the Muskwa Assemblage are generally quite poor. Cross-cutting diabase dikes related to the Gunbarrel large igneous province provide a minimum age constraint (U-Pb baddeleyite) for the basin of 779 ± 2 Ma (LeCheminant and Heaman, 1994). Ross and others (2001) conducted a detrital zircon provenance study on the lower half of the exposed succession that yielded youngest zircon grain ages of 1766 ± 14 Ma, 1783 ± 26 Ma and 1843 ± 14 Ma for the lower Tuchodi

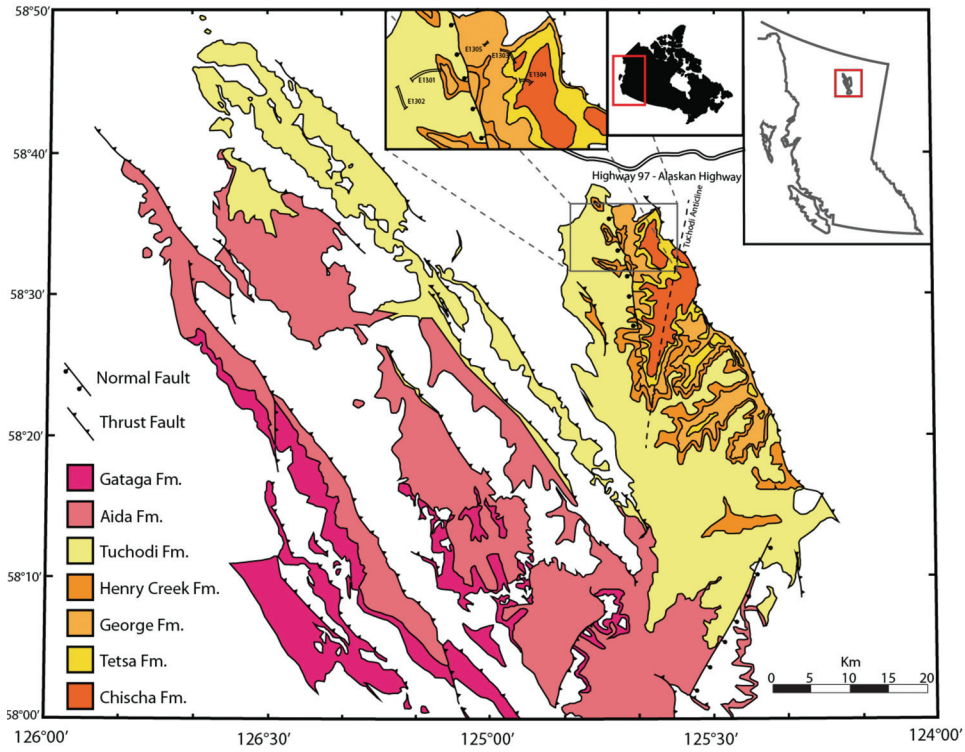

Fig. 1. Generalized geological map of the Muskwa Assemblage including section localities. The lower part of the assemblage is only exposed along the Tuchodi anticline to the north-east and accessible from the Alaskan Highway (upper-right). The upper section of the basin is exposed on the western limb of the anti-cline, along with a set of east-verging thrust faults and west-dipping normal faults. Modified from Taylor and Stott (1973).

Fm., and upper and lower Chischa Fm., respectively (fig. 2). Detrital zircon age distributions from the same study (Ross and others, 2001) resemble those from the Athabasca Basin (Rainbird and others, 2007) and the Wernecke Supergroup (Furlanetto and others, 2016), prompting the interpretation that these basins were all correlative and may have formed a continuous passive margin surrounding Laurentia (Ross and others, 2001; Furlanetto and others, 2016). The 1.40 to 1.47 Ma Belt-Purcell Basin (Evans and others, 2000) located further south in the Cordillera, along the Canada-US border has also been considered a correlative unit due to its lithologic similarity (Taylor and Stott, 1973). The basal units of the Belt-Purcell Supergroup (Pre-Missoula Group) have similar detrital zircon age distributions to the Muskwa Assemblage (Ross and Villeneuve, 2003). Though the succession is at least clearly mid-Proterozoic (~1.76–1.4 Ga) and thus adds to the limited number of thick, well-exposed units in this time interval, it is clear that additional work is needed to resolve the age of the Muskwa Assemblage.

METHODS

Sampling

Five stratigraphic sections covering over 2 km of stratigraphy were measured through the lower stratigraphy of the Muskwa Assemblage (fig. 3). Across these

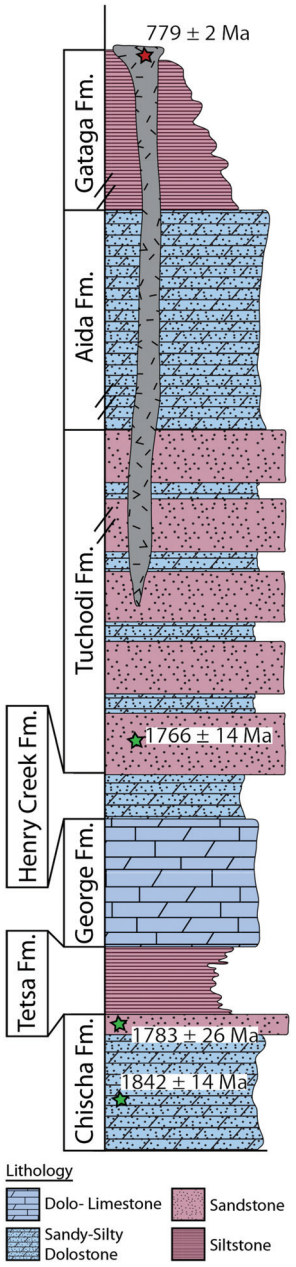

Fig. 2. Generalized lithologic stratigraphy of the Muskwa Assemblage (Bell, 1968). Absolute age constraints for the basin are broad, defined by detrital zircon ages in the basal units (green stars, Ross and others, 2001) and U-Pb Baddeleyite ages from crosscutting gabbro dikes (red star, LeCheminant and Heaman, 1994). Figure modified from Ross and others (2001).

sections, 237 samples were collected for geochemical analysis from the Chischa, Tetsa, George, and Tuchodi formations. Carbonates were sampled at 3 to 5 m intervals where sufficiently exposed, and care was taken to avoid heavily weathered surfaces, fault

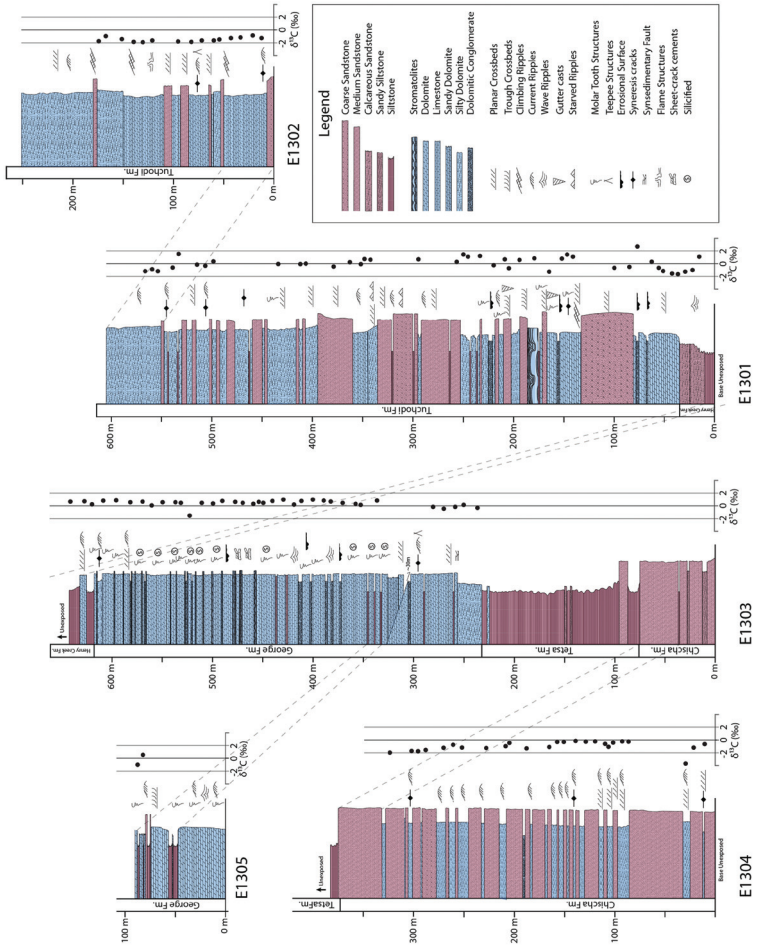

Fig. 3. Detailed stratigraphic columns of all measured sections, including carbon isotope results. The section comprises a continuous transect of the Chischa Fm., the Tetsa Fm. and the George Fm., correlating across a valley (Sections E1304 and E1303). A second transect was measured across the lower Tuchodi Fm., correlating across along a mountain face (Sections E1301 and E1302).

contacts, contact metamorphism from dikes, and generally heavily reworked carbonates with fabric disruption. Samples were cut into billets and petrographically assessed for veining, recrystallization and other signs of alteration. Selected samples were then micro-drilled using a tungsten carbide micro-drill bit, avoiding veining and clear signs of alteration.

Analytical Methods

Carbonate samples were measured for major, trace, and rare earth elements at the Yale Metal Geochemistry Center in a Pico-trace clean lab. Wet chemical treatment of samples was carried out in acid-cleaned plastics and Teflon beakers. Sample powders were weighed out into 1.5 ml microcentrifuge tubes (6–8 mg of powder) and dissolved using three consecutive 1.5 ml 0.35 M HCl leaches. For each leach, samples were reacted for 1 hour, 30 minutes and 10 minutes, respectively, centrifuged and the supernatant was then removed to be dried. Dissolved samples were dried down in clean

Teflon beakers and subsequently dissolved in 5 percent HNO_3 for major, trace and REE+Y analysis using a Thermo Element XR ICP-MS.

A small subset of samples for each facies was selected for a sequential leaching procedure. Samples were dissolved using a modified 5 step leaching method that chemically separates calcite and dolomite phases from silicates due to their different dissolution rates (modified from Tostevin and others, 2016). Samples were weighed into 1.5 ml centrifuge tubes (~ 10 mg of powder) and leached using the following steps: one step of 1 ml 1 M ammonium acetate (Step N1) and four steps of 1 ml 0.35 M HCl (S1-S4). For each step, samples were dissolved for 15 minutes, centrifuged, and the supernatant was then removed using a clean pipette. The supernatant for each leach step was dried down in a clean Teflon beaker and then dissolved in 5 percent HNO_3 for major element, trace element and REE+Y analysis.

Analytical standards were made in-house using single element standards and were made to match the typical concentration range of Proterozoic carbonates. Geological standards (USGS COQ-1 carbonatite and USGS BHVO-2 basalt) were run alongside samples. Both standards were within 10 percent of reported values, with most elements within 5 percent of reported values. Multi-run lab errors for each element are included with REE and trace element data (tables 1, 2 and 3).

Carbon isotope ($\delta^{13}C$) and oxygen isotope ($\delta^{18}O$) analysis were performed using a dual inlet Nu Instruments Perspective IRMS at the Department of Earth and Planetary Sciences at McGill University coupled to a NuCarb automated carbonate preparation device. Samples were weighed into acid cleaned glass sample vials, heated for 24 hours to dry, and then reacted with phosphoric acid at 70 °C for analysis. All values are reported relative to VPDB (Vienna Pee Dee Belemnite) delta notation. Precision for $\delta^{13}C$ and $\delta^{18}O$ are 0.024 permil and 0.042 permil (2-σ), respectively, based on repeat analyses of standards.

All REE+Y data are normalized to Post-Archean Australian Shale (PAAS; Taylor and McLennan, 1985). Although PAAS REE+Y values have recently been reviewed (Pourmand and others, 2012), and there are new estimates to modern upper continental crustal REE+Y values (for example MuQ; Kamber and others, 2005), we normalize our REE+Y values to PAAS as calculated by Taylor and McLennan (1985) to maintain consistency with the large record of previous REE+Y studies.

STRATIGRAPHY AND PETROGRAPHY

Basin Stratigraphy

The basic stratigraphy of the Muskwa Assemblage was broadly defined during initial mapping of the area (Bell, ms 1966, 1968; Taylor and Stott, 1973). We measured and correlated 5 sections (fig. 3) and took 237 carbonate samples from the lower carbonate-rich units of the Muskwa Assemblage. Of those samples, 20 were selected for detailed petrographic analysis and cathodoluminescence microscopy (CL) (figs. 4A–4F). Below is a description of sedimentological and stratigraphic observations for each unit, integrating previous work where applicable.

Chischa Formation.—The Chischa Fm. is a mixed siliciclastic-carbonate sequence that outcrops within the core of the Tuchodi Anticline along the Tetsa and Chischa rivers (fig. 1). The base of the unit is not exposed in the area (Bell, 1968). The formation is broadly composed of 2 to 5 m-thick, pale gray, fine-grained quartz arenite beds interbedded with laminated sandy and silty fine-grained dolomite. Quartz arenite beds have well-developed wave ripples and planar cross-bedding throughout the unit. Carbonate beds in the lower half of the unit are generally finely crystalline dolomite with few sedimentary structures. Beds in the upper member are similar but contain minor, thin 10 to 15 cm thick carbonate conglomerate beds, slump structures, and beds with minor amounts of molar tooth structures (MTS). Carbonate conglomerate

TABLE 1

$\delta^{13}C$ and $\delta^{18}O$ values for whole rock carbonates from units across the Muskwa Assemblage

Sample	Unit	$\delta^{13}C$ (‰)	$\delta^{18}O$ (‰)	Sample	Unit	$\delta^{13}C$ (‰)	$\delta^{18}O$ (‰)
E1301-432.6	Tuchodi Fm.	0.04	-11.90	E1302-120.9 REP	Tuchodi Fm.	-1.69	-9.43
E1301-203.5	Tuchodi Fm.	-0.67	-16.21	E1302-130.5	Tuchodi Fm.	-1.88	-8.76
E1301-140.8	Tuchodi Fm.	1.14	-9.16	E1302-140	Tuchodi Fm.	-1.74	-9.45
E1301-340.6	Tuchodi Fm.	0.74	-11.50	E1302-152	Tuchodi Fm.	-1.43	-8.08
E1301-179.6	Tuchodi Fm.	0.85	-9.38	E1302-165	Tuchodi Fm.	-0.94	-11.21
E1301-361.4	Tuchodi Fm.	0.26	-8.21	E1302-174.8	Tuchodi Fm.	-1.61	-7.58
E1301-550.9	Tuchodi Fm.	-1.15	-11.40	E1302-181.9	Tuchodi Fm.	-1.77	-8.91
E1301-84.3	Tuchodi Fm.	-0.53	-11.51	E1302-21.4	Tuchodi Fm.	-0.96	-10.90
E1301-99	Tuchodi Fm.	-0.63	-7.52	E1302-33.2	Tuchodi Fm.	-1.12	-10.69
E1301-496.1	Tuchodi Fm.	0.45	-11.40	E1302-42.6	Tuchodi Fm.	-1.27	-11.15
E1301-56.6	Tuchodi Fm.	-0.58	-7.17	E1302-54.2	Tuchodi Fm.	-1.44	-11.97
E1301-505.2	Tuchodi Fm.	-0.28	-12.38	E1302-54.2 REP	Tuchodi Fm.	-1.42	-11.96
E1301-557.1	Tuchodi Fm.	-0.89	-11.05	E1302-60.7	Tuchodi Fm.	-1.62	-11.24
E1301-42.7	Tuchodi Fm.	-1.49	-9.80	E1302-72.6	Tuchodi Fm.	-1.57	-11.80
E1301-244.3	Tuchodi Fm.	1.13	-12.36	E1302-82.3	Tuchodi Fm.	-1.72	-11.64
E1301-346.3	Tuchodi Fm.	0.77	-11.03	E1302-95.5	Tuchodi Fm.	-1.87	-10.82
E1301-537.2	Tuchodi Fm.	-0.66	-11.63	E1303-249.7	George Fm.	0.17	-10.64
E1301-145.9	Tuchodi Fm.	1.45	-10.31	E1303-258.2	George Fm.	-0.19	-13.05
E1301-29.9	Tuchodi Fm.	-1.33	-8.39	E1303-269.3	George Fm.	-0.42	-15.95
E1301-405.1	Tuchodi Fm.	0.07	-11.35	E1303-280.2	George Fm.	-0.14	-12.71
E1301-254.7	Tuchodi Fm.	0.28	-13.29	E1303-335.8	George Fm.	0.90	-10.10
E1301-51	Tuchodi Fm.	-1.11	-11.60	E1303-352.1	George Fm.	0.21	-10.05
E1301-512.7	Tuchodi Fm.	-0.09	-12.21	E1303-357.2	George Fm.	0.37	-12.83
E1301-22.7	Tuchodi Fm.	-1.00	-9.23	E1303-370.4	George Fm.	0.54	-13.79
E1301-564	Tuchodi Fm.	-1.09	-11.32	E1303-381.9	George Fm.	0.61	-11.20
E1301-37.7	Tuchodi Fm.	-1.70	-12.40	E1303-389	George Fm.	0.78	-10.67
E1301-208	Tuchodi Fm.	0.70	-14.50	E1303-399.6	George Fm.	0.97	-11.29
E1301-249.1	Tuchodi Fm.	1.44	-12.79	E1303-411.4	George Fm.	0.70	-11.28
E1291-193.1	Tuchodi Fm.	0.53	-12.77	E1303-418.0	George Fm.	0.23	-12.49
E1301-410.4	Tuchodi Fm.	0.05	-11.50	E1303-429.2	George Fm.	1.00	-8.72
E1301-232.7	Tuchodi Fm.	1.24	-14.09	E1303-440.1	George Fm.	0.76	-10.80
E1301-76.4	Tuchodi Fm.	2.69	-1.27	E1303-449.2	George Fm.	0.50	-11.89
E1301-350.7	Tuchodi Fm.	-0.02	-9.40	E1303-459.3	George Fm.	0.27	-11.82
E1301-293.6	Tuchodi Fm.	0.67	-12.13	E1303-469.7	George Fm.	0.49	-10.31
E1301-15.1	Tuchodi Fm.	1.14	-12.23	E1303-477.4	George Fm.	0.65	-11.96
E1301-163.8	Tuchodi Fm.	-1.12	-9.06	E1303-490.0	George Fm.	0.72	-9.48
E1301-531	Tuchodi Fm.	1.57	-12.27	E1303-499.1	George Fm.	0.43	-10.38
E1301-377.6	Tuchodi Fm.	-0.34	-12.16	E1303-510.4	George Fm.	0.42	-13.38
E1301-62.5	Tuchodi Fm.	0.29	-11.08	E1303-522.8	George Fm.	-1.49	-6.45
E1301-218.7	Tuchodi Fm.	-0.18	-9.34	E1303-531.6	George Fm.	0.49	-4.82
E1301-151.4	Tuchodi Fm.	0.72	-14.84	E1303-536.6	George Fm.	0.62	-9.32
E1302-101.4	Tuchodi Fm.	-2.05	-10.22	E1303-549.2	George Fm.	0.55	-12.73
E1302-110.4	Tuchodi Fm.	-2.00	-10.30	E1303-560.5	George Fm.	0.03	-10.68
E1302-12.3	Tuchodi Fm.	-1.18	-11.95	E1303-569.3	George Fm.	0.71	-8.80
E1302-120.9	Tuchodi Fm.	-1.71	-9.55	E1303-581.6	George Fm.	0.55	-10.23
E1303-595.6	George Fm.	0.88	-12.10	E1304-209	Chischa Fm.	-0.39	-9.23
E1303-609.0	George Fm.	0.82	-10.26	E1304-213.0	Chischa Fm.	-0.94	-11.75
E1303-620.4	George Fm.	0.26	-10.39	E1304-22.3	Chischa Fm.	-1.13	-9.20
E1303-627.4	George Fm.	0.71	-9.49	E1304-232.7	Chischa Fm.	-1.26	-11.67
E1303-641.3	George Fm.	0.66	-8.84	E1304-257.1	Chischa Fm.	-1.12	-10.67

TABLE 1
(continued)

Sample	Unit	$\delta^{13}C$ (‰)	$\delta^{18}O$ (‰)	Sample	Unit	$\delta^{13}C$ (‰)	$\delta^{18}O$ (‰)
E1303-651.5	George Fm.	0.67	-8.13	E1304-265.9	Chischa Fm.	-0.72	-8.54
E1303-656	George Fm.	0.75	-11.78	E1304-275.6	Chischa Fm.	-1.13	-9.84
E1303-667.3	George Fm.	1.08	-12.78	E1304-293.9	Chischa Fm.	-1.44	-10.01
E1303-674.0	George Fm.	0.02	-7.79	E1304-30.0	Chischa Fm.	-3.62	-14.89
E1303-678.0	George Fm.	1.38	-9.45	E1304-301.6	Chischa Fm.	-1.73	-8.34
E1304-10.8	Chischa Fm.	-0.65	-12.53	E1304-307.8	Chischa Fm.	-1.75	-9.28
E1304-104.1	Chischa Fm.	-0.40	-12.51	E1304-329.5	Chischa Fm.	-1.91	-10.24
E1304-108.9	Chischa Fm.	-0.93	-12.80	E1304-88.0	Chischa Fm.	-0.22	-10.64
E1304-111.6	Chischa Fm.	-0.64	-9.99	E1304-94.4	Chischa Fm.	-0.22	-10.35
E1304-121.83	Chischa Fm.	-0.14	-10.16	E1305-82.2	George Fm.	0.62	-10.14
E1304-131.4	Chischa Fm.	-0.23	-7.97	E1305-86.6	George Fm.	-0.99	-11.05
E1304-141.9	Chischa Fm.	-0.11	-7.93	E1304-153.8	Chischa Fm.	-0.30	-8.57
E1304-153.8	Chischa Fm.	-0.30	-8.57	E1304-160.6	Chischa Fm.	-0.29	-9.29
E1304-160.6	Chischa Fm.	-0.29	-9.29	E1304-168.7	Chischa Fm.	-1.08	-11.28
E1304-168.7	Chischa Fm.	-1.08	-11.28	E1304-191.4	Chischa Fm.	-1.31	-9.37
E1304-191.4	Chischa Fm.	-1.31	-9.37	E1304-209	Chischa Fm.	-0.39	-9.23

beds are generally clast-supported with coarse angular to sub-angular flat-pebbled carbonate clasts.

In thin section, carbonate lithologies are mainly composed of a structureless, fine-grained and finely crystalline dolomite matrix with varying abundances of rounded feldspar and quartz sand grains (fig. 4A). Under cathodoluminescent microscopy, the carbonate matrix is generally dull-luminescent. However, coarser-grained sandier sediments show some brightly-luminescent, late-stage dolomite cements that fill intergranular porosity. Siliciclastic material within this finely crystalline matrix is generally composed of mixed fine- to medium-grained feldspar and quartz, which is moderately sorted and sub-rounded to rounded.

Tetsa Formation.—The Tetsa Fm. is a fine-grained, dominantly siliciclastic unit overlying the Chischa Fm. The base of the Tetsa Fm. is gradational with the underlying Chischa Fm. At the contact, medium-grained, pale gray quartz arenite is interlaminated with fine, dark gray to black siltstone. Thinly-laminated, dark gray to black siltstone progressively becomes the dominant lithology over a 25 m interval and then comprises most of the remaining Tetsa Fm. The top of the formation shows a transition with increasing fine-grained dolomite beds interbedded with the siltstone over ~ 35 m below the contact with the George Fm. Siltstones across the Tetsa Fm. show no distinct mechanical sedimentary structures and are generally planar laminated. Finely crystalline dolomite shows weakly developed laminations, and beds near the top of the formation contain small, weakly asymmetric stratified ripples.

George Formation.—The George Fm. is a dominantly carbonate unit composed of bedded, fine-grained dolomite and limestone, with stromatolites and carbonate conglomerates. Unlike other units across the Muskwa Assemblage, the George Fm. contains only minimal siliciclastic detrital material.

The base of the George Fm. is characterized by a progressive loss of the finely-bedded siltstones typical of the Tetsa Fm. and an increase in thickly bedded, sandy dolomite with climbing ripples and lenticular bedding. This transitions over 20 m to finely crystalline and weakly laminated dolomites interbedded with clast-supported,

TABLE 2

Major and trace element concentrations for whole rock carbonates from units across the Muskwa Assemblage

Sample	Facies	Mg (ppm)	Al (ppm)	Ca (ppm)	Mn (ppm)	Fe (ppm)	Rb (ppm)	Sr (ppm)
E1301-47.6	Tuchodi Fm.	146400	2295	200700	619	8041.6	7.96	38.2
E1301-84.3	Tuchodi Fm.	43100	1077	308400	304	5341.6	1.61	69.6
E1301-99.0	Tuchodi Fm.	147200	1183	208700	1600	9799	4.19	42.2
E1301-140.8	Tuchodi Fm.	146000	597	193700	1234	6983.5	1.53	32.6
E1301-145.9	Tuchodi Fm.	142400	2407	211900	835	10485.4	6.94	55.5
E1301-151.4	Tuchodi Fm.	18500	454	376100	327	350.5	1.42	144.9
E1301-163.8	Tuchodi Fm.	91600	2977	227600	497	9726.6	3.58	150.8
E1301-179.6	Tuchodi Fm.	142000	2739	206600	727	14273.9	6.79	70
E1301-208	Tuchodi Fm.	149200	991	202000	679	9193.7	2.25	31.5
E1301-232.7	Tuchodi Fm.	130700	3088	186500	874	14574.6	5.34	38.1
E1301-244.3	Tuchodi Fm.	126300	2267	185300	1052	13528.8	2.33	35.5
E1301-293.6	Tuchodi Fm.	123300	3173	181300	1024	12498.5	3.62	33.2
E1301-346.3	Tuchodi Fm.	146800	1581	200200	866	10138.5	4.61	37.1
E1301-361.4	Tuchodi Fm.	147600	2204	201800	843	9767.3	5.95	42.2
E1301-377.6	Tuchodi Fm.	141000	1043	200400	829	9301.9	0.91	38.3
E1301-410.4	Tuchodi Fm.	144300	2323	193100	845	11179.6	6.92	30.6
E1301-432.6	Tuchodi Fm.	138200	2265	204800	964	13162.8	5.93	63.1
E1301-490.1	Tuchodi Fm.	12500	231	380200	242	161.9	0.63	72.1
E1301-505.2	Tuchodi Fm.	140900	3707	177600	1209	18723.7	10.3	40.1
E1301-531.6	Tuchodi Fm.	143000	1853	192300	1839	10914.8	6.34	32.9
E1301-557.1	Tuchodi Fm.	110300	540	196800	560	856.8	0.99	27.7
E1301-564	Tuchodi Fm.	146800	2641	196400	1083	10707.5	8.13	35
E1302-21.7	Tuchodi Fm.	155000	2837	217000	855	10911.7	9.48	55.7
E1302-33.2	Tuchodi Fm.	137700	1883	183400	848	8007.7	4.35	39.6
E1302-42.6	Tuchodi Fm.	167600	4998	223100	814	13820.9	20.21	74.5
E1302-72.6	Tuchodi Fm.	168900	1924	232400	706	9003.1	7.55	51.8
E1302-82.3	Tuchodi Fm.	165800	1931	231500	748	12472.4	9.76	63.2
E1302-95.5	Tuchodi Fm.	136800	1330	197600	702	8004	2.08	40.4
E1302-101.4	Tuchodi Fm.	121700	1736	220800	992	1727.3	4.71	61.3
E1302-120.9	Tuchodi Fm.	137800	1966	193400	776	2077.4	6.92	59
E1302-130.5	Tuchodi Fm.	151400	2264	198100	611	7629.2	6.77	45.6
E1302-140.0	Tuchodi Fm.	164800	2854	226600	668	10824.7	11.79	56.4
E1302-152.0	Tuchodi Fm.	135100	2158	194300	627	7479.7	3.24	42.4
E1302-168	Tuchodi Fm.	123400	879	186400	1073	1367.4	3.61	32.9
E1303-227.1	George Fm.	123200	1407	204400	881	13612.6	1.31	44.3
E1303-249.7	George Fm.	99700	8113	209600	561	12096.7	25.56	27.4
E1303-258.2	George Fm.	167700	1305	240300	764	12284.8	3.29	58.5
E1303-269.3	George Fm.	154500	1296	218500	491	6543.7	3.54	36.2
E1303-280.2	George Fm.	154200	1353	216200	592	10684.4	2.35	46.8
E1303-335.8	George Fm.	160400	2139	226200	912	11786.9	5.18	44.5
E1303-357.2	George Fm.	120400	792	222600	518	1737.6	1.82	39
E1303-364.1	George Fm.	134000	715	196200	513	10994.9	1.42	30.3
E1303-389	George Fm.	111600	961	234400	617	1745.2	2.68	56.1
E1303-399.6	George Fm.	58200	606	311200	511	808.8	3.08	128.1
E1303-411.4	George Fm.	58100	555	341600	266	4322.1	1.86	93.8
E1303-418	George Fm.	7400	343	391300	201	190.6	1.06	97.4
E1303-449.2	George Fm.	9500	156	367000	114	1028.1	0.6	96.8
E1303-469.7	George Fm.	59600	1071	320700	354	450.6	2.05	244.2
E1303-477.4	George Fm.	4600	72	373200	102	559	0.52	114.6
E1303-485	George Fm.	131900	633	197200	701	752.9	1.15	33.5

TABLE 2
(continued)

Sample	Facies	Mg (ppm)	Al (ppm)	Ca (ppm)	Mn (ppm)	Fe (ppm)	Rb (ppm)	Sr (ppm)
E1303-490	George Fm.	97400	1562	289100	236	4348	2.99	71.7
E1303-499.1	George Fm.	54500	639	340400	194	2931.1	1.84	87.1
E1303-507.1	George Fm.	134900	181	199000	1209	7321.5	0.06	21
E1303-510.4	George Fm.	123100	368	220400	589	630.1	0.63	28.5
E1303-522.8	George Fm.	152800	671	201900	2051	4393.7	1.2	47.2
E1303-531.6	George Fm.	149000	797	202600	486	3169.1	1.54	41.9
E1303-534.4	George Fm.	35300	171	334600	288	176.6	0.4	91.3
E1303-536.6	George Fm.	91500	769	308800	305	3181.3	0.87	84
E1303-549.2	George Fm.	152100	281	202900	642	5055	0.62	24.1
E1303-552.9	George Fm.	122700	296	218700	687	942.3	0.46	27.2
E1303-560.5	George Fm.	36500	769	360200	133	2201.5	1.7	87.4
E1303-569.7	George Fm.	96300	1016	289000	201	3644.9	2.49	103.3
E1303-577.7	George Fm.	9200	173	373900	134	126.8	0.48	182.9
E1303-581.6	George Fm.	53900	510	329100	202	2996.8	1.75	105.8
E1303-595.6	George Fm.	64900	837	333900	322	4388.8	3.26	75.4
E1303-609	George Fm.	34900	738	359400	175	1701.2	1.6	178.8
E1303-620.4	George Fm.	14000	264	387000	130	1404.9	0.68	86.3
E1303-627.4	George Fm.	63700	593	326000	215	3296.6	1.36	179.9
E1303-641.3	George Fm.	154000	2439	205200	602	5844.7	5.1	42.2
E1303-651.5	George Fm.	114800	510	271400	441	3280.5	1.19	76
E1303-656	George Fm.	169400	231	216000	525	6986.5	1.03	26.3
E1303-667.3	George Fm.	145500	227	176200	538	9896.9	0.57	23.1
E1303-674.0	George Fm.	118700	1825	230200	381	9477.2	5.26	72.9
E1303-678.0	George Fm.	47900	726	305400	345	5441.9	2.08	101.6
E1304-10.8	Chischa Fm.	153700	1407	207900	317	5354.1	3.46	30.8
E1304-30.0	Chischa Fm.	133400	1994	193700	314	6536.4	2.71	35.9
E1304-94.4	Chischa Fm.	149600	5038	200700	291	8038.2	16.68	39.2
E1304-104.1	Chischa Fm.	149400	368	174300	257	6342.8	1.14	22.8
E1304-121.8	Chischa Fm.	153000	3232	215500	290	5617.5	8.76	41.4
E1304-131.4	Chischa Fm.	155400	999	207600	331	5096.7	2.19	32.3
E1304-134.7	Chischa Fm.	124800	1343	175900	381	7755	1.93	54.3
E1304-141.9	Chischa Fm.	152900	1060	178200	290	8459.4	3.18	43.3
E1304-153.8	Chischa Fm.	153700	1581	211400	334	6425.9	4.38	46.7
E1304-191.6	Chischa Fm.	142900	1052	187000	476	1131	2.32	32.9
E1304-209	Chischa Fm.	150300	2982	203900	352	6516.6	6.88	44.4
E1304-213.0	Chischa Fm.	150500	2368	199000	404	7596.9	5.06	46.8
E1304-232.7	Chischa Fm.	128200	1404	192800	354	5655.9	1.72	46.1
E1304-265.9	Chischa Fm.	150000	416	177900	255	6115.6	1.29	25.9
E1304-275.6	Chischa Fm.	135400	5157	183600	449	1797.1	10.73	45.4
E1304-293.9	Chischa Fm.	150700	1831	207600	355	6374.7	4.32	38.8
E1304-301.6	Chischa Fm.	146800	1601	205900	318	6342.3	3.5	28.2
E1305-19.9	George Fm.	26800	990	328600	188	3485.3	4.37	83.7
E1305-72	George Fm.	23500	1016	388600	130	1675.5	2.73	68
E1305-82.2	George Fm.	107500	638	304200	391	7625.4	2.26	62.2
E1305-86.6	George Fm.	117400	2485	276100	358	8125.9	5.08	57.8
	Blank	0.971	0.593	10.047	0.27	0.721	0.006	0.062
	Error (2-σ)	103.8	6.25	420.25	2.21	0.3	0.02	0.14

TABLE 3

Rare Earth Element and Yttrium (REE+Y) concentrations for whole rock carbonates from units across the Muskwa Assemblage

Sample	Unit	La (ppm)	Ce (ppm)	Pr (ppm)	Nd (ppm)	Sm (ppm)	Eu (ppm)	Gd (ppm)	Dy (ppm)	Y (ppm)	Ho (ppm)	Er (ppm)	Tm (ppm)	Yb (ppm)
E1301-84.3	Tuchodi Fm.	21.5	43.28	5.39	26.26	5	0.93	5.236	4.08	23.9	0.73	2.14	0.26	1.86
E1301-140.8	Tuchodi Fm.	9.4	19.84	1.91	7.01	1.3	0.26	1.315	0.95	6.05	0.18	0.5	0.07	0.43
E1301-151.4	Tuchodi Fm.	16.2	28.7	2.96	10.44	1.8	0.35	1.736	1.18	7.73	0.22	0.6	0.08	0.48
E1301-163.8	Tuchodi Fm.	15.5	33.28	4.57	22.65	4.8	0.91	4.775	4.35	23.96	0.81	2.47	0.29	2.26
E1301-244.3	Tuchodi Fm.	11.3	28.88	4.02	21.06	4.9	1.04	5.135	4.79	25.11	0.86	2.42	0.27	1.97
E1301-293.6	Tuchodi Fm.	7	19.58	2.52	13.66	3.9	0.83	3.912	3.81	21.84	0.68	2.01	0.25	1.71
E1301-377.6	Tuchodi Fm.	7.5	20.69	2.86	14.28	3.3	0.66	3.281	2.87	18.09	0.52	1.48	0.17	1.22
E1301-432.6	Tuchodi Fm.	20.4	47.22	5.84	24.55	6.1	1.41	6.657	5.93	38.11	1.11	2.9	0.39	2.17
E1301-505.2	Tuchodi Fm.	23.6	52.05	5.93	23.3	5	1.12	5.122	4.28	26.89	0.81	2.11	0.29	1.68
E1301-557.1	Tuchodi Fm.	8.4	25.21	3.29	16.46	4.3	1	3.841	4.36	21.87	0.82	2.09	0.28	1.78
E1302-95.5	Tuchodi Fm.	11.4	30.64	3.95	20.33	4.8	1.05	5.172	4.63	28.67	0.8	2.31	0.25	1.82
E1302-101.4	Tuchodi Fm.	9.6	28.09	4.3	17.45	5.2	0.97	4.918	5.82	32.98	1.05	2.92	0.33	2.22
E1302-152.0	Tuchodi Fm.	9.6	24.68	3.09	14.77	3.6	0.67	3.411	3.62	20.11	0.65	1.68	0.23	1.42
E1302-168	Tuchodi Fm.	6.9	19.54	2.28	9.74	2.9	0.71	3.231	2.86	14.8	0.52	1.37	0.15	1.16
E1303-227.1	George Fm.	12.9	33.95	4.41	22.45	4.5	0.91	4.184	3.9	22.32	0.7	1.8	0.24	1.46
E1303-357.2	George Fm.	9	23.24	3.4	12.64	3	0.38	2.597	2.39	13.68	0.42	1.06	0.12	0.83
E1303-364.1	George Fm.	6.7	13.95	1.82	7.02	1.6	0.36	1.756	0.92	5.15	0.16	0.42	0.05	0.36
E1303-399.6	George Fm.	2.9	5.37	0.57	2.12	0.4	0.09	0.426	0.29	2.12	0.05	0.16	0.02	0.14
E1303-418	George Fm.	9.1	15.53	1.83	6.43	1.1	0.24	1.003	0.73	5.12	0.14	0.39	0.05	0.31
E1303-449.2	George Fm.	10.4	17.41	1.91	6.67	1.1	0.19	1.065	0.74	6.22	0.15	0.4	0.06	0.33
E1303-477.4	George Fm.	5.9	8.74	0.9	3.12	0.5	0.11	0.536	0.41	4.55	0.08	0.25	0.04	0.22
E1303-485	George Fm.	8.7	15.72	1.74	6.15	1	0.16	1.078	0.58	4.14	0.11	0.3	0.03	0.26
E1303-507.1	George Fm.	4.7	8	0.87	3.26	0.7	0.14	0.86	0.66	5.48	0.14	0.4	0.05	0.39
E1303-534.4	George Fm.	4.8	8.19	0.91	3.26	0.6	0.12	0.654	0.44	3.83	0.09	0.25	0.03	0.22
E1303-536.6	George Fm.	5.6	10.28	1.34	5	1	0.19	0.898	0.7	4.87	0.14	0.34	0.06	0.33
E1303-552.9	George Fm.	6.1	11.85	1.54	5.55	1.3	0.21	1.216	0.95	6.21	0.06	0.49	0.06	0.43
E1303-577.7	George Fm.	3.1	5.63	0.56	1.97	0.4	0.08	0.377	0.29	2.66	0.06	0.16	0.02	0.15
E1303-667.3	George Fm.	7	12.59	1.48	5.21	1	0.2	0.903	0.59	4.4	0.11	0.29	0.04	0.24
E1303-674.0	George Fm.	22	44.72	4.86	17.51	3.2	0.47	2.682	1.77	10.47	0.31	0.81	0.11	0.65
E1303-678.0	George Fm.	6	10.94	1.33	5.26	0.9	0.18	0.819	0.72	6.31	0.14	0.38	0.07	0.37
E1304-30.0	Chischa Fm.	6.3	15.7	2.33	9.9	2.2	0.42	1.789	1.78	9.61	0.32	0.84	0.13	0.74
E1304-104.1	Chischa Fm.	4.8	11.81	1.6	6.76	2	0.52	2.25	1.82	12.04	0.33	0.84	0.11	0.69
E1304-134.7	Chischa Fm.	2.5	9.4	1.53	7.51	2.4	0.55	2.009	2.32	11.97	0.4	0.96	0.13	0.91
E1304-141.9	Chischa Fm.	5.9	16.19	1.88	8.07	2.2	0.49	2.211	1.88	10.92	0.34	0.84	0.12	0.69
E1304-191.6	Chischa Fm.	1.8	6.16	0.82	3.87	1.7	0.42	1.622	1.42	8.12	0.24	0.62	0.07	0.49
E1304-232.7	Chischa Fm.	2.5	8.04	1.46	7.65	3.5	1.12	3.3	3.03	16.53	0.53	1.23	0.18	1.07
E1304-265.9	Chischa Fm.	2.5	9.41	1.33	5.94	1.8	0.45	1.756	1.49	8.48	0.26	0.7	0.09	0.55
E1305-19.9	George Fm.	30.1	56.53	5.77	20.82	1.8	0.6	3.571	2.67	17.53	0.51	1.4	0.2	1.27
E1305-72	George Fm.	16.5	28.29	3.03	10.47	1.7	0.27	1.571	0.96	5.83	0.17	0.46	0.06	0.38
Blank		0.005	0.009	0.001	0.014	0.001	0.006	0.008	0.001	0	0.004	0	0	0.001
Error (2σ)		0.201	0.015	0.084	0.015	0.135	0.013	0.002	0.085	0.016	0.081	0.024	0.023	0.025

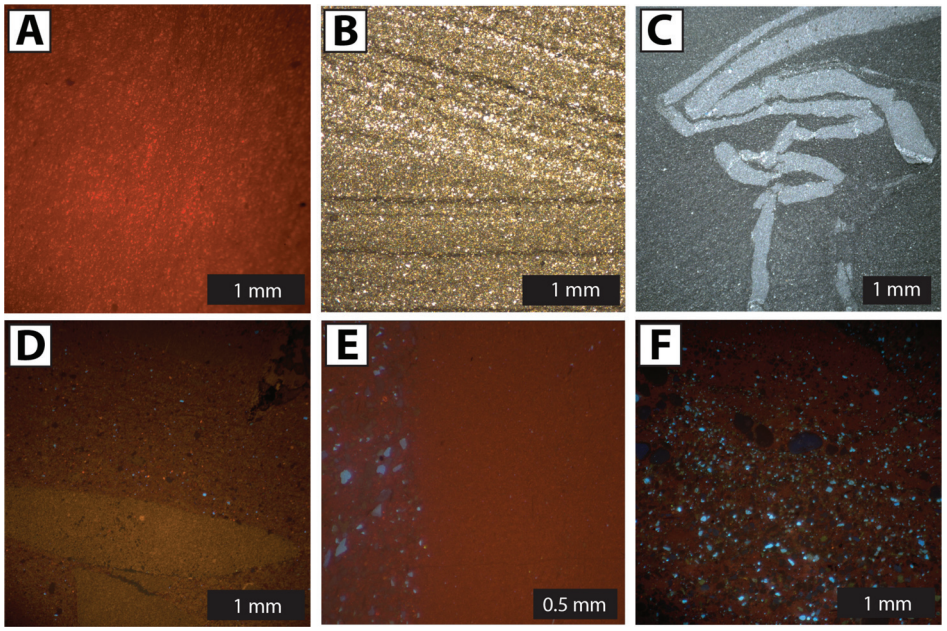

Fig. 4. (A) Dominantly dull-luminescent, finely crystalline dolomite with minor interstitial bright-luminescent dolomite crystals, typical of dolomite samples with high carbonate content – Chischa Fm., CL. (B) Truncation surface in thinly laminated, finely crystalline dolomite – George Fm., PPL. (C) Discretely laminated, finely crystalline dolomite and silt matrix folding around broken and deformed calcite MTS veins – George Fm., PPL (plain polarized light). (D) Finely crystalline calcite matrix with minor disseminated dull-luminescent dolomite replacement as well as bright luminescent dolomite and silicate silt. MTS veins (lower, yellow fragments) are composed largely of finely crystalline calcite – George Fm., CL. (E) Dull-luminescent, finely crystalline dolomite with fine sand layers (rich in bright-blue luminescent feldspars) defining the discrete laminations – Tuchodi Fm., CL (cathodoluminescence). (F) Sandy dolomite typical of lower- to mid-ramp facies. Feldspar (bright blue) and quartz grains (non-luminescent) are rounded and moderately sorted. Interspersed among the sand grains are rare bright-luminescent dolomite grains and crystals – Tuchodi Fm., CL.

flat-pebbled carbonate conglomerates (fig. 5A). In these lithologies, dolomite occurs as both fine grains (generally bright-luminescent under CL) and finely crystalline material with poorly- to well-developed rhombic crystal forms and dull luminescence (fig. 4B).

The middle George Fm. contains less siliciclastic content than the base, concurrent with an increased abundance of carbonate conglomerate beds and the occurrence of both symmetric and asymmetric ripples (fig. 5B), and soft-sediment deformation features (fig. 5C). The upper George Fm. is characterized by the appearance of stromatolites (fig. 5D), abundant molar tooth structures (fig. 4C) and fine-grained limestone. The uppermost 25 m of the George Fm. is distinguished by an abrupt increase in siliciclastic material. These silty and sandy fine-grained dolomite beds mark a gradual transition into the overlying Henry Creek Fm.

Whereas limestone is generally uncommon in the sequence, it does occur in individual 5 to 10 m thick, discontinuous, fine-grained limestone beds in the upper George Fm. In thin section, these limestones are composed of finely crystalline calcite micrite with minor microcrystalline dolomite interspersed within the dominant calcite matrix (fig. 4D). Finely crystalline dolomites are generally dull-luminescent but rare bright-luminescent grains are sometimes present in the matrix.

Stromatolites within the George Fm. form small, low-relief mounds (<10 m wide) developed within fine-grained and finely-crystalline carbonate beds (fig. 5D). The

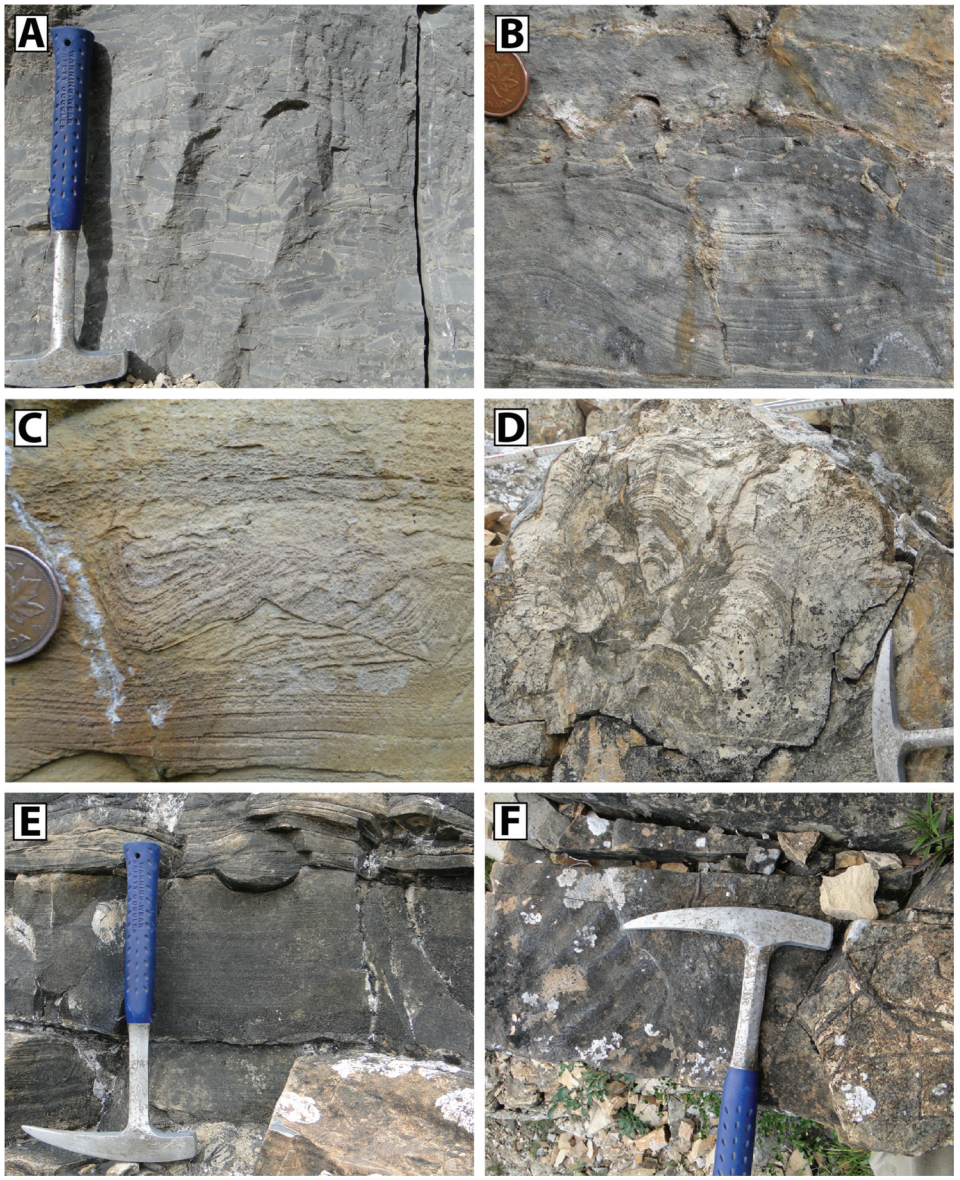

Fig. 5. (A) Carbonate conglomerate flow, typically formed with a basal scour and overlain by fine draping micrites. Clasts are typically dolomite within a finely crystalline dolomite matrix – George Fm. (B) Stacked slightly asymmetric wave-ripple crossbedding – George Fm. (C) Syn-sedimentary micro-faulting and deformation in sandy dolomite – lower George Fm. (D) Low-relief domal stromatolite mound. Domal dolomite columns are discretely laminated and tightly packed. Rare sediment infill between columns is finely crystalline dolomite – George Fm. (E) Laminated sandy, finely crystalline dolomite with a scour mark – Tuchodi Fm. (F) Wave ripples in sandy dolomite. Though rare in most of the lower units, both are extensive in the upper Tuchodi Fm – Tuchodi Fm.

stromatolites form as tightly packed 30 to 50 cm wide columns, which are discretely laminated and contain rare sediment infill between columns. The stromatolitic mounds are not commonly vertically stacked, but instead typically form discontinuous,

1 to 5 m-thick bioherms that are no more than 10 m wide. MTS are extensive in the upper George Fm., predominantly forming in fine-grained carbonate beds, which in places have been erosionally truncated. The molar tooth structures commonly occur as swarms of ptygmatically folded and deformed calcite microspar-filled cracks. In thin section, the MTS appear broken and deformed (fig. 4C), and the finely-crystalline laminated carbonate sediments hosting the structures deform around the more rigid MTS calcite infill (fig. 4D). Under cathodoluminescence, MTS infill appears to be composed of very finely crystalline calcite, which has a non-luminescent, rounded core overgrown by a brightly luminescent phase. MTS beds are often silicified, with dark-brown chert replacing molar tooth fill and the surrounding carbonate. This silicification occurs either as thin microcrystalline rims along the edge of MTS veins or later more pervasive replacement that overprints depositional textures. Overall, MTS in the George Fm. have consistent features with other known localities in the Proterozoic (Smith, 2016). Though rare, minor bedding parallel sheet-cracks with fibrous carbonate cement (distinct from molar tooth structures) also occur within carbonate beds of the upper George Fm.

Henry Creek Formation.—The Henry Creek Fm. is dominantly composed of sandy and silty dolomite, interbedded with siltstone in the lower parts of the unit. The base of the Henry Creek Fm. is transitional from the George Fm., as carbonate beds become increasingly silty and more discrete beds of dark gray siltstone appear. The Henry Creek Fm. was not studied here in detail, but Bell (ms 1966, 1968) and Aitken and McMechan (1991) describe the lower part of the formation as interbedded sandy, fine-grained dolomite and dark gray siltstone, with the upper part of the formation characterized by sandy fine-grained dolomite interbedded with sandstone. Overall, the Henry Creek Fm. is increasingly dominated by quartz sands upwards and the contact with the overlying Tuchodi Fm. is marked by the first appearance of thick white quartz arenite beds (Bell, ms 1966).

Tuchodi Formation.—The Tuchodi Fm. is the most extensively exposed unit across the basin (fig. 1) and dominated by sandstones and sandy dolomites. The lower 200 m of the Tuchodi Fm. is characterized by interbedded sandstone and fine-grained dolomite (fig. 5E), including interbedded carbonate conglomerates, MTS and rare thin stromatolite beds. Stromatolites form broad 0.5 to 1.0 m domal mounds, but unlike those in the George Fm., stromatolites within the Tuchodi Fm. have a thinner, markedly branched column morphology with a tuberous shape and steeply convex laminations. MTS within the lower Tuchodi Fm. are similar to those of the George Fm. but are not silicified. Generally, the carbonates of the lower Tuchodi Fm. are sandy and silty finely-crystalline dolomites (fig. 4E). In thin section, sub-rounded to rounded, fine- to medium-grained feldspar and quartz grains are common and form alternating finer and coarser grained laminations of the same dominant composition (fig. 4F). The carbonate matrix is mainly composed of finely crystalline dull-luminescent dolomite with minor, rounded dull-luminescent calcite grains, and some bright-luminescent zoned calcite.

The middle and upper Tuchodi Fm. is composed of sandy, fine-grained dolomite and medium-grained sandstones similar to those of the lower Tuchodi Fm., often interbedded with thick 5 to 30 m planar cross-bedded quartz arenites. These middle and upper units often contain wave ripples (fig. 5F), syneresis cracks, starved ripples, load casts and fluid escape structures.

Here we only documented the lower 800 m of the Tuchodi Fm., which is estimated elsewhere to be up to 1500 m. The middle and upper sections of the formation are lithologically similar to the lower section, dominated by thick coarse sandstone interbedded with sandy and silty dolomite (Bell, 1968).

Gataga and Aida Formations.—The Aida and Gataga Fm. are fine-grained siliciclastic formations overlying the Tuchodi Fm. These formations were not the subject of this study but have been studied by Bell (ms 1966, 1968), we briefly summarize that work here. Bell describes the Aida Fm. as a thick succession of dominantly brown to gray weathered, slaty and calcareous siltstone and mudstone. Soft-sediment deformation structures and thin, occasionally graded, poorly sorted sandstones are typical. Within the mid-Aida Fm. are two prominent marker beds: a 55 m thick green-chamosite mudstone unit overlain by a 60 m thick carbonaceous mudstone unit. The overlying Gataga Fm. consists of moderately recessive, dark-gray to dark-olive green siltstones and mudstones. In contrast to the underlying Aida Fm., it is generally devoid of carbonate and coarser siliciclastics (Bell, ms 1966). Only minor thin sandstone units are present, which typically accompany flame structures and contorted mudstone or siltstone laminations. The top of the Gataga Fm. is eroded and unconformably overlain by the Early Cambrian Atan Group (Bell, ms 1966).

It is important to note that the Gataga Fm. exposed within the Muskwa Assemblage is not to be confused with similar named Cryogenian units exposed to the west of the Tuchodi Lakes map area in the Gataga Mt area (Ferri and others, 1999; Colpron and others, 2002). Bell (ms 1966, 1968) interpreted a conformable contact between the Gataga Fm. and the underlying Aida Fm. and made the observation that these units were crosscut by the same Gunbarrel aged dikes which crosscut most of the Muskwa Assemblage. Thus, these units are without a doubt part of the Muskwa Assemblage and should not be misinterpreted with Neoproterozoic aged units further west.

GEOCHEMICAL RESULTS

Carbon and Oxygen Isotopes

A composite $\delta^{13}C$ and $\delta^{18}O$ dataset was generated from 66 screened samples across the Chischa Fm., George Fm., and the lower Tuchodi Fm., representing the majority of the exposed carbonate strata within the basin (table 1). $\delta^{13}C$ and $\delta^{18}O$ were measured on samples at roughly 10 to 15 m intervals where carbonate samples were available (fig. 3). Overall, $\delta^{13}C$ values range from -3.63 permil to 2.69 permil with most samples lying between roughly -2.00 permil and 1.50 permil. Carbonate $\delta^{13}C$ values show a systematic variability between each formation. The upper George Fm. and the lower Tuchodi Fm. record generally positive $\delta^{13}C$ values with the highest measured values in the sequence (median of 0.55 ‰; fig. 6). In contrast, the Chischa Fm. and the upper Tuchodi Fm. both record some of the lowest $\delta^{13}C$ values (median of -0.70 ‰; fig. 6).

Across the basin, $\delta^{18}O$ values range between -16.20 permil to -4.80 permil (not including a single outlier of -1.27 ‰) but generally show little variability between different formations or facies. The $\delta^{18}O$ values across the basin have a narrow range (median of -10.60 ‰, stdev of 2.04 ‰). These values broadly fall within typical values for the Proterozoic (Shields and Veizer, 2002), and do not show any correlation with $\delta^{13}C$ for either individual formations or overall, across the basin ($R^2 < 0.1$; fig. 6).

Major, Trace, and Rare Earth Element Data

Major and trace element concentrations were measured on 97 carbonate samples across the Chischa Fm., George Fm. and Tuchodi Fm. (tables 2 and 3). After petrographic screening and major and trace element work, we selected a subset of 39 samples for REE+Y analysis. Of these samples, 7 are limestone samples (<5% Mg-calcite) and 17 are dolomitic limestone samples (5–25% Mg-calcite), with the remaining samples being dolomite (>25% Mg-calcite), as determined by Mg/Ca ratios. The limestone and dolomitic limestone samples were exclusively found in the upper George Fm. and a narrow stratigraphic range within the lower Tuchodi Fm.

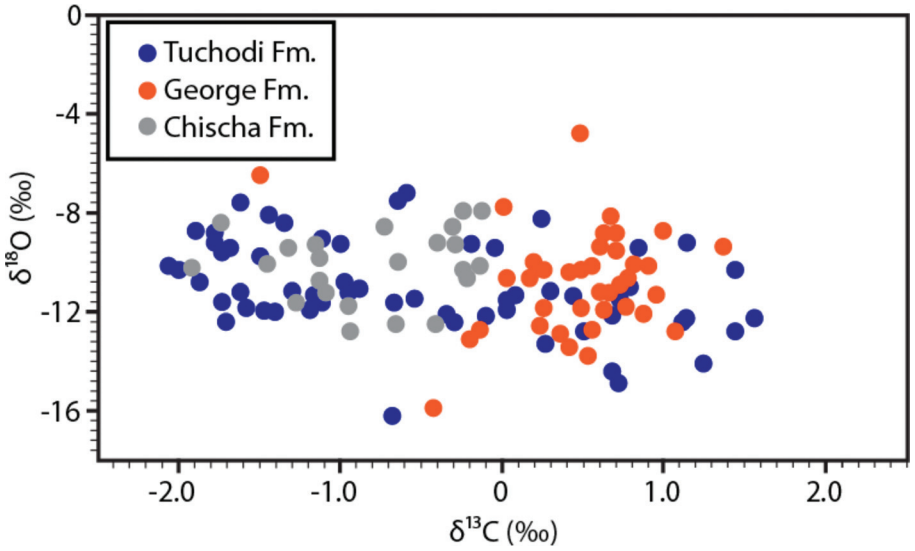

Fig. 6. Carbon isotopes and oxygen isotope results for the Tuchodi, George, and Chischa Fm. No correlation was found between the carbon and oxygen isotopes either in individual formations or across the Muskwa Assemblage.

Shale-normalized (PAAS; Taylor and McLennan, 1985) REE+Y profiles appear to be distinct between different stratigraphic units. The upper George Fm. and the lower Tuchodi Fm. record generally flat REE patterns with a slight light REE+Y (LREE) enrichment (La/Yb normalized to PAAS, La/Yb range 0.89–2.50, average 1.78). In addition, these units have negative Ce anomalies [Ce/Ce* = Ce/(Pr (Pr/Nd)); range 0.86 – 1.17, average 1.0; Lawrence and others 2006]. In the upper Tuchodi Fm. and the basal George Fm. we observe a strong LREE depletion (range 0.30–1.36, average 0.61) with a wide range but generally positive Ce/Ce* values (range 0.79–1.31, average 1.10). In the Chischa Fm. we observe similar patterns to the upper Tuchodi Fm. and basal George Fm., large LREE depletions (range 0.17–0.63, average 0.39) but a much narrower range of Ce/Ce* (range 0.89–1.14, average 0.99).

We compare REE+Y values with $\delta^{13}C$, $\delta^{18}O$ and major and trace element values and find that La/Yb and Ce/Ce* do not show any significant correlation with $\delta^{18}O$, [Rb] and Mg/Ca (fig. 7). We did find, however, that Ce/Ce* correlates strongly with $\delta^{13}C$ in the upper and mid ramp facies (fig. 8B).

Major, trace and REE+Y concentrations were also measured in four sequentially leached samples selected from different formations and facies (tables 4 and 5) of which three were dolomite samples and one was a limestone. In all sequentially leached samples, REE+Y patterns in the initial ammonium acetate leaching step (N1) had REE+Y below the detection limit and are, therefore, not included. Our sequentially leached samples are not mass corrected as we cannot measure the mass of dissolved carbonate between each leaching step, therefore we use Ca and Mg concentrations from each step to scale REE+Y concentrations to a theoretical Mg and Ca sum of 35 percent to account for variable carbonate dissolution in each step. For all four samples, despite some minor variation in REE+Y concentrations between steps, REE+Y patterns and concentrations for each sample step are both strikingly similar to bulk leached values (fig. 9). In addition, we calculate composite REE+Y values for each sample by adding together the concentration for each sample's first three leaching

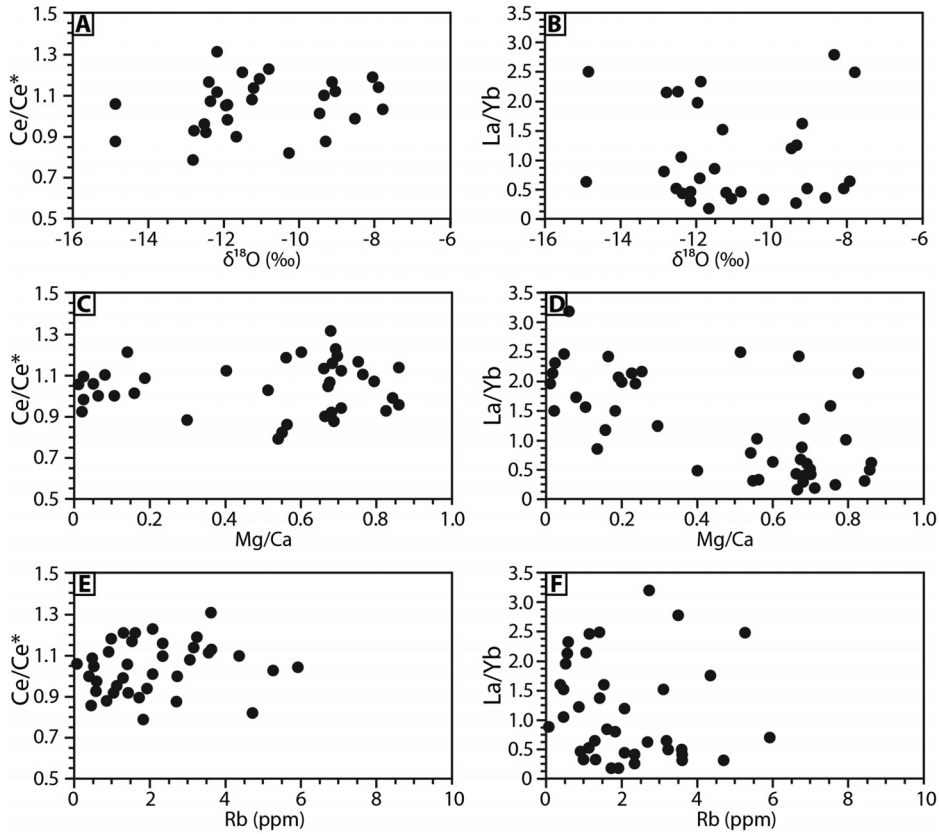

Fig. 7. Geochemical plots highlighting alteration proxies from carbonates of the Muskwa Assemblage. (A) A comparison of carbonate $\delta^{18}O$ and Ce/Ce* do not show any strong correlations. (B) Similarly, comparing $\delta^{18}O$ and La/Yb, there are no strong correlations. (C) Comparison of Ce/Ce* with Mg/Ca shows minimal correlation. (D) Comparison between Mg/Ca and La/Yb, shows no correlation. (E) Ce/Ce* does not have a strong correlation with Rb concentration, nor is there any tapering of Ce/Ce* values towards 1.0 with increasing Rb concentrations. (F) Similar to Ce/Ce*, there is little shift in La/Yb values with increasing Rb concentrations.

steps (S1-S3). We compare this to each sample's cleanest step (S3; Tostevin and others, 2016) and find similar results suggesting that the small variations in concentrations in initial leaching steps do not impact overall REE+Y patterns (fig. 9).

DISCUSSION

Basin Architecture, Stratigraphy, and Paleo-environmental Evolution

The dominantly carbonate lower Muskwa Assemblage records the development of a carbonate ramp along a western facing margin (Bell, ms 1966, 1968; Long and others, 1999). The lower Tuchodi Fm. and the George Fm. record largely carbonate facies, whereas the Chischa Fm., Tetsa Fm. and the upper Tuchodi Fm. are mixed carbonate and siliciclastic lithologies (fig. 3). Utilizing carbonate and siliciclastic sedimentology, and placing these units within a stratigraphic context, we define three broad paleo-depth facies for the Muskwa Assemblage, from a deep marine lower ramp to a mid-ramp, and upper ramp setting.

In what we interpret as the deepest marine facies assemblage of the basin, the Tetsa Fm. and lower Henry Creek Fm. both consist of interbedded siltstone and

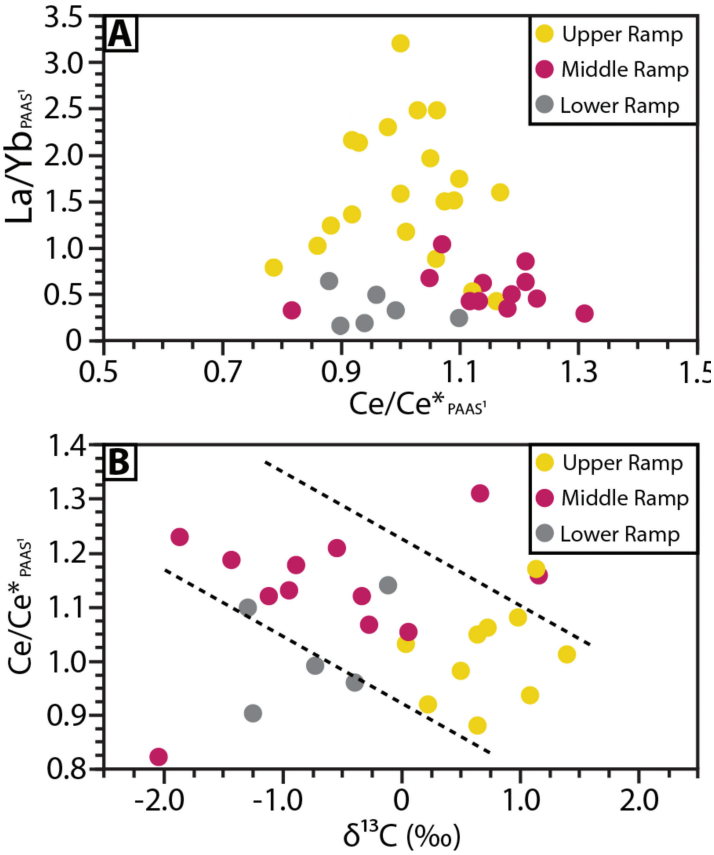

Fig. 8. (A) Ce*/Ce anomalies show a narrow range of values relative to modern environments across the Muskwa Assemblage (0.86–1.36). Ce anomalies show no clear correlation with LREE depletion between facies or across the basin. (B) Ce anomalies are tightly correlated to $\delta^{13}C$ in shallow and mid- ramp facies but not with deeper lower ramp facies.

fine-grained dolomite. These sediments are fine-grained and laminated, likely suggesting relatively low-energy conditions on the distal portion of a ramp. This facies preserves little to no indication of reworking by storm, tidal or wave action. The lack of turbidites and other ramp-derived structures suggests limited shoreward slope development. Transitions from these deeper water, middle to lower ramp facies into shallower upper ramp settings (for example the Tetsa Fm. to lower George Fm.) show progressively greater carbonate content upwards and increasing amounts of physical sediment reworking.

The lower and middle George Fm., the uppermost Chischa Fm., and the upper Tuchodi Fm. are interpreted to represent a mid-ramp setting, likely near the fair-weather wave base but certainly above storm-wave base facies. These facies are characterized by coarser, more calcareous sediments influenced by traction currents. These units often comprise silty and sandy dolomites rather than pure carbonates (fig. 5E), suggesting the influence of a nearby clastic system. Fine-grained and finely-crystalline dolomites contain occasional soft-sediment deformation structures and flame structures (fig. 5C). Fine-grained carbonates and interbedded siliciclastics contain both wave and current ripples (fig. 5F) indicating active sediment reworking

TABLE 4

Major and trace element concentrations for a selection of sequentially leached whole rock carbonates from units across the Muskwa Assemblage

Sample	Leaching Step	Mg (ppm)	Al (ppm)	Ca (ppm)	Mn (ppm)	Fe (ppm)	Rb (ppm)	Sr (ppm)
E1303-418	S1	-	-	-	-	-	-	-
	S2	8100	72	345400	125	1105.8	0.15	82
	S3	10700	201	153600	71	1481.5	0.32	34.2
	S4	3900	94	81200	25	422	0.22	11
E1304-104.1	S1	136000	167	189200	277	4630.7	0.42	25.3
	S2	116500	374	159600	215	4033.1	0.21	17.4
	S3	88900	223	132500	152	3271.3	0.19	13.2
	S4	50100	165	92400	84	2196.9	0.22	6.5
E1301-163.8	S1	48400	4370	189300	316	6155.9	5.41	151.8
	S2	23900	2892	89200	132	3299.3	2.32	42.8
	S3	11200	1678	29300	54	2013.8	1.24	10.2
	S4	3400	645	6700	12	609.7	0.62	2.6
E1303-536.6	S1	53000	165	262900	171	2651.6	0.58	84.4
	S2	60800	510	265100	193	3214.7	0.31	75.8
	S3	76800	958	167900	198	3394.7	0.35	36
	S4	30100	403	70000	72	1621.6	0.28	7.5
	Blank	0.971	0.593	10.047	0.27	0.721	0.006	0.062
	Error (2-σ)	103.8	6.25	420.25	2.21	0.3	0.02	0.14

by wave action and storm wave action. These features likely derive from a higher energy environment above storm-wave base, probably near fair weather wave base. Tabular beds of clast-supported, coarse flat-pebbled carbonate conglomerate beds (fig. 5A) and finer-grained graded beds are common. These carbonate conglomerate beds are often capped by climbing ripples, reflecting potential storm reworking and a high-energy environment. Based on the range of lithologies, from silty carbonates, debrites, and wave rippled sands, this facies association probably represents a mid-ramp setting, influenced by intermittently high-energy processes. Many planar cross-bedded and wave-rippled sand beds occur in what is interpreted as the shallowest sections of this facies, likely straddled across storm-wave base and fair-weather wave base. In contrast, the lower part of this middle ramp facies is characterized by silty and sandy carbonates receiving abundant sediment influx from the upper ramp, and commonly reworked by storm- and fair-weather wave action.

A stratigraphically thin portion of the lower George Fm, the upper George Fm. and the lower Tuchodi Fm. are interpreted to encompass the shallowest marine environments of the Muskwa Assemblage, with deposition above fair-weather wave base. This facies contains clean carbonates with cross-bedding, stromatolites (fig. 5D), MTS (fig. 4C), and preserves limestone lithologies. The lack of debris deposits and soft-sediment deformation structures in these formations coincides with the development of stromatolitic units and MTS. Silicification and MTS are usually associated with shallow water settings in Precambrian basins (Shields, 2002; Maliva and others, 2005; Smith, 2016), with MTS typically restricted to sub-tidal facies (O'Connor, 1972; James and others, 1998). Taken together, these features indicate a more stable but higher energy environment, likely placing this facies in a shallower upper ramp environment. Though it is difficult to estimate a precise water depth, there are no clear sub-aerial

TABLE 5

Rare Earth Element and Yttrium (REE+Y) concentrations for selection of sequentially leached whole rock carbonates from units across the Muskwa Assemblage

Sample	Leaching Step	La (ppm)	Ce (ppm)	Pr (ppm)	Nd (ppm)	Sm (ppm)	Eu (ppm)	Gd (ppm	Dy (ppm)	Y (ppm)	Ho (ppm)	Er (ppm)	Tm (ppm)	Yb (ppm)
E1303-418	S1	-	-	-	-	-	-	-	-	-	-	-	-	-
	S2	9.8	16.89	2.06	6.94	1.3	0.25	1.128	0.61	5.7	0.15	0.36	0.06	0.28
	S3	4.2	9.06	1.08	3.93	0.6	0.13	0.612	0.44	3.1	0.08	0.2	0.03	0.1
	S4	1	2.18	0.3	1.09	0.2	0.05	0.165	0.1	0.65	0.02	0.06	0.01	0.04
E1304-104.1	S1	1.9	4	0.52	2.24	0.6	0.17	0.752	0.67	5.43	0.13	0.37	0.04	0.28
	S2	2.9	7.04	1.2	4.7	1.5	0.42	1.593	1.36	7.21	0.24	0.61	0.07	0.48
	S3	1.6	4.26	0.57	2.45	0.6	0.16	0.712	0.64	4.94	0.12	0.29	0.04	0.24
	S4	0.8	2.08	0.28	1.15	0.4	0.1	0.371	0.33	2.16	0.06	0.16	0.02	0.12
E1301-163.8	S1	9.1	20.87	2.55	11	2.5	0.51	2.377	2.37	13.22	0.45	1.23	0.16	1.15
	S2	3.5	8.33	1.07	4.6	1	0.23	1.026	1.01	5.18	0.19	0.52	0.06	0.46
	S3	1.3	3.74	0.41	2	0.5	0.09	0.46	0.38	1.78	0.07	0.18	0.03	0.19
	S4	0.3	0.96	0.13	0.48	0.1	0.02	0.099	0.07	0.54	0.02	0.04	0.01	0.04
E1303-536.6	S1	1.4	1.53	0.13	0.5	0.1	0.02	0.087	0.07	0.83	0.02	0.05	0.01	0.04
	S2	4.8	8.76	0.93	3.96	0.8	0.14	0.67	0.53	3.85	0.1	0.3	0.04	0.29
	S3	3.1	6.56	0.75	2.88	0.5	0.1	0.448	0.37	2.56	0.07	0.17	0.03	0.16
	S4	0.7	1.57	0.16	0.67	0.1	0.03	0.116	0.11	0.54	0.05	0.05	0.01	0.05
Blank		0.005	0.009	0.001	0.014	0.001	0.006	0.008	0.001	0	0.004	0	0	0.001
Error (2-σ)		0.201	0.015	0.084	0.015	0.135	0.013	0.002	0.08	0.016	0.081	0.024	0.023	0.025

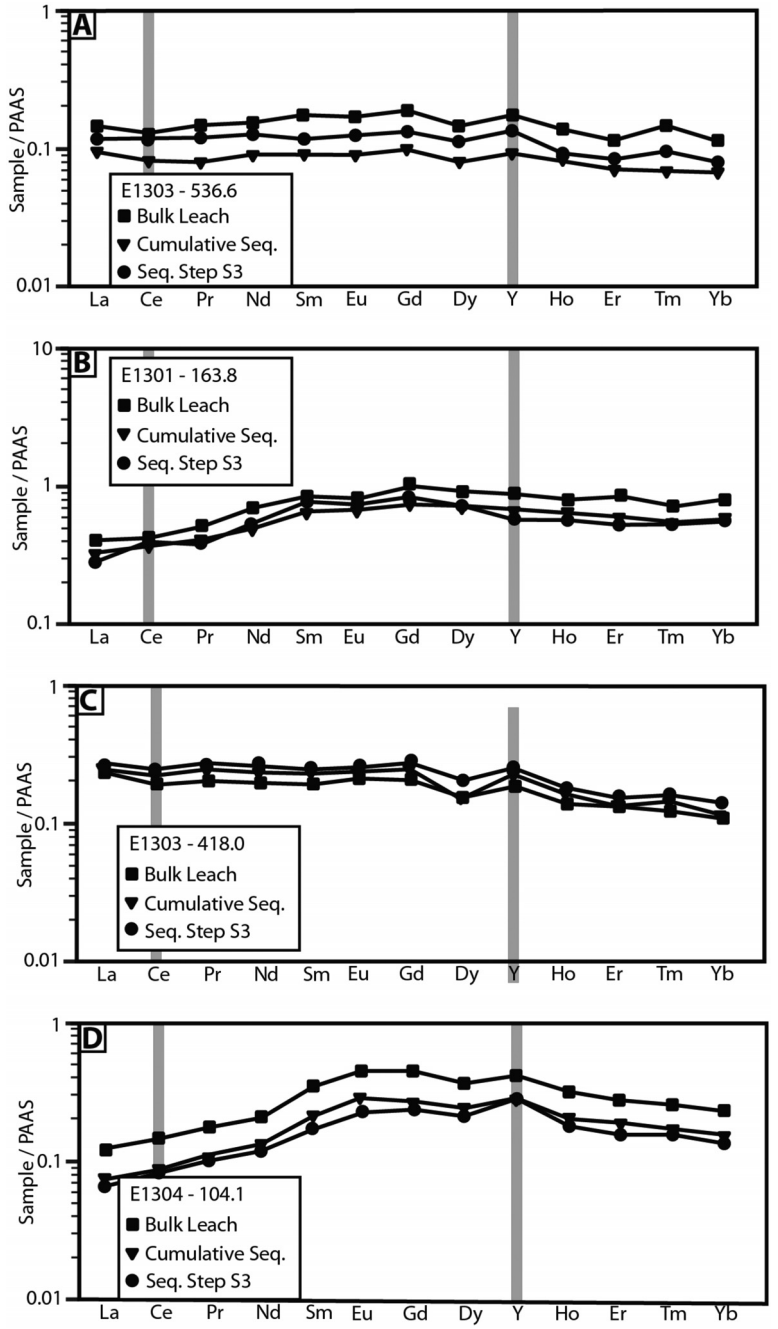

Fig. 9. A comparison of bulk leached REE+Y patterns to sequentially leached REE+Y patterns. For each sequentially leached sample we scaled REE+Y concentrations to a theoretical Mg and Ca sum of 35% to account for variable carbonate dissolution in each step. Sequential leaching step S3, which is considered the cleanest step (Tostevin and others, 2016), does not show any significant deviation from bulk leached REE+Y values for all four samples. Additionally for each sample, a cumulative composite REE+Y value was calculated by adding together the concentration for each sample's first three leaching steps (S1-S3). There is little difference in REE+Y values and concentration between each, which indicates that early leaching steps do not impact overall REE+Y patterns.

exposure features (for example mudcracks, teepee structures) or a long-term exposure surface (for example karst development), suggesting a persistently subaqueous environment.

Placing these three facies paleo-depth constraints within stratigraphic context, these facies transitions appear to form two cyclic sequences in the basal five formations of the Muskwa Assemblage. The upper Chischa Fm. records an initial basin deepening, followed by the first regressive sequence occurring from the Tetsa Fm. To the top of the George Fm, with a smaller order regressive-transgressive sequence in the lower George Fm. This is then followed by a sharp transgression in the basal Henry Creek Fm. The second sequence consists of a more rapid shallowing from the lower Henry Creek Fm. To a maximum regressive surface in the lower Tuchodi Fm. Above this, the upper Tuchodi Fm., Aida Fm. and Gataga Fm. appear to be distinct from this cyclic sedimentation pattern. The upper Tuchodi Fm. contains far more abundant coarse-grained siliciclastics than the lower units of the Muskwa Assemblage, and both the Aida and Gataga Fm. are dominantly fine-grained siliciclastics with little to no carbonate present. They appear to show a general transgressive trend, with the Gataga Fm. containing mainly deep water, fine-grained sediments (Bell, ms 1966). It is unclear what drives the cyclicity of the basal five formations (for example eustatic sea-level change or periodic basin subsidence), however, the departure from this cyclicity marks an important shift in either local tectonics or sedimentary source.

Rare Earth Element Geochemistry

REE+ Y preservation.—Marine carbonates have been found to be a reliable archive of seawater REE+Y (for example Liu and Schmitt, 1984; Sholkovitz and Shen, 1995). Even in cases of minor diagenesis or dolomitization, empirical studies have found samples can reliably retain primary REE+Y patterns (Banner and others, 1988b; Kamber and Webb, 2001; Bau and Alexander, 2006). REE+Y have a high calcite-seawater partitioning coefficient compared to many other elements (>100; Zhong and Mucci, 1995), making REE+Y less sensitive to secondary fluid-rich diagenesis, including dolomitization (Zhao and Zheng, 2017). However, there are some examples of significant post-depositional carbonate REE+Y alteration (for example Nothdurft and others, 2004; Zhao and Zheng, 2017). Therefore, it is imperative that samples are individually assessed for primary REE+Y signal preservation (Tostevin and others, 2016). We evaluate samples for alteration from meteoric diagenesis, dolomitization, and dissolution of detrital material.

Meteoric diagenesis and dolomitization are of particular concern for the Muskwa Assemblage. This is because dolomite is the most common carbonate mineralogy within the Muskwa Assemblage, and low $\delta^{18}O$ values may suggest some secondary meteoric diagenesis. Many dolomitic units, where dolomitization occurs both early and late in the paragenetic sequence, have been found to reliably retain REE+Y patterns during dolomite replacement (Banner and others, 1988b; Bau and Alexander, 2006). REE+Y preservation is likely due to a combination of a high rock buffering capacity, a marine Mg source during dolomite replacement, which can help lead to retention of marine trace metal chemistry (Wacey and others, 2007; Kenward and others, 2009; Hood and Wallace, 2014), and minimal contamination from clays and oxide dissolution (Liu and Schmitt, 1984; Shaw and Wasserberg, 1985; Elderfield and Sholkovitz, 1987; Haley and others, 2004). However, fabric destructive dolomitization can alter REE+Y patterns of the precursor limestone if the dolomitizing (or subsequent) fluids have a very different REE+Y concentrations and distributions compared to seawater-derived fluids (for example Nothdurft and others, 2004). The timing of dolomitization in the Muskwa Assemblage is not well-constrained. However, the dolomitization is largely fabric-retentive and in thin section, dolomitized limestone lithologies are

not coarsely-crystalline (crystal size less than 50 μm). Fabric-retentive dolomitization often occurs during early diagenesis, with a fluid derived largely from seawater (for example Tucker, 1983), suggesting that Muskwa dolomitization was potentially early and could have retained primary REE+Y signatures. Additionally, we find that dolomite and limestone samples both preserve similar LREE enriched REE+Y pattern in upper ramp settings (fig. 10C) and LREE depleted REE+Y patterns in lower and middle ramp settings (figs. 10A–10B). While Ce/Ce* and La/Yb show no strong correlation with Mg/Ca values (figs. 7C–7D), they show nearly a full range of values at both low and high Mg/Ca values. Thus, while Muskwa Assemblage carbonates may have undergone minor secondary fluid-rich diagenesis, the range of REE+Y patterns observed does not appear to be controlled by the dolomitizing fluid.

Silicate material is another common source of REE+Y contamination (Nothdurft and others, 2004; Tostevin and others, 2016). During carbonate sample dissolution detrital clays and silicate minerals can be inadvertently dissolved, incorporating terrigenous REE+Y into solution and contaminating carbonate REE+Y values (Bailey and others, 2000; Liu and others, 2013; Tostevin and others, 2016). In addition, detrital sourced REE+Y may also be incorporated into carbonate crystals during diagenesis (Liu and Schmitt, 1984; Shaw and Wasserberg, 1985). We attempt to track the extent of these processes using [Rb] concentrations. As Rb is released during silicate and clay dissolution (Banner and others, 1988a; Bailey and others, 2000), but is also incorporated into the carbonate lattice during recrystallization, it can track terrigenous contamination during diagenesis. Comparing Ce/Ce* and La/Yb to Rb concentrations, we see no systematic shift in REE+Y patterns (figs. 7E–7F), suggesting that terrigenous input is minor and has not significantly altered REE+Y patterns.

To further ensure we are measuring primary REE+Y profiles, we measured REE+Y on several sequentially leached samples, which has emerged as a more thorough dissolution method (for example Tostevin and others, 2016) We compare the best-preserved leaching steps to bulk leached samples and see little difference in actual REE+Y patterns and in their respective Ce/Ce* and La/Yb values (fig. 9).

Non-traditional REE+Y alteration proxies.—In addition to the more traditional carbonate alteration and detrital contamination proxies (Mn/Sr, [Rb]), there is a growing use of a number of non-traditional alteration proxies to identify REE+Y preservation. In particular, total REE+Y concentrations (ΣREE+Y), Y/Ho ratios and middle REE+Y enrichment (MREE; Chen and others 2015; Satkoski and others, 2016), have all been used to try and identify primary carbonate REE+Y samples. Applying these to assess Precambrian carbonates REE+Y preservation present some problems, however, as these proxies rely on assumptions about modern seawater REE+Y cycling.

For instance, Y/Ho ratios have emerged as a tool to track detrital contamination in carbonate REE+Y measurements. As modern oxic seawater has a high Y/Ho (~60–90) and detrital clays and silicates have Y/Ho values near Upper Continental Crust (~27–30; Taylor and McLennan, 1985), low Y/Ho values in Phanerozoic carbonate REE+Y measurements have been interpreted to indicate detrital contamination (Zhao and others, 2013). The Y/Ho enriched in modern seawater, however, is due to the preferential removal of REE relative to Y by Fe-Mn oxyhydroxides in oxic conditions (Bau and others, 1997; Bau, 1999). In modern anoxic basins, such as the hypersaline Tyro sub-Basin, large Y/Ho enrichments are restricted to within surface oxic waters and deeper anoxic waters do not preserve any Y/Ho enrichment (Bau and others, 1997). Therefore, it should be expected that Mid-Proterozoic seawater likely

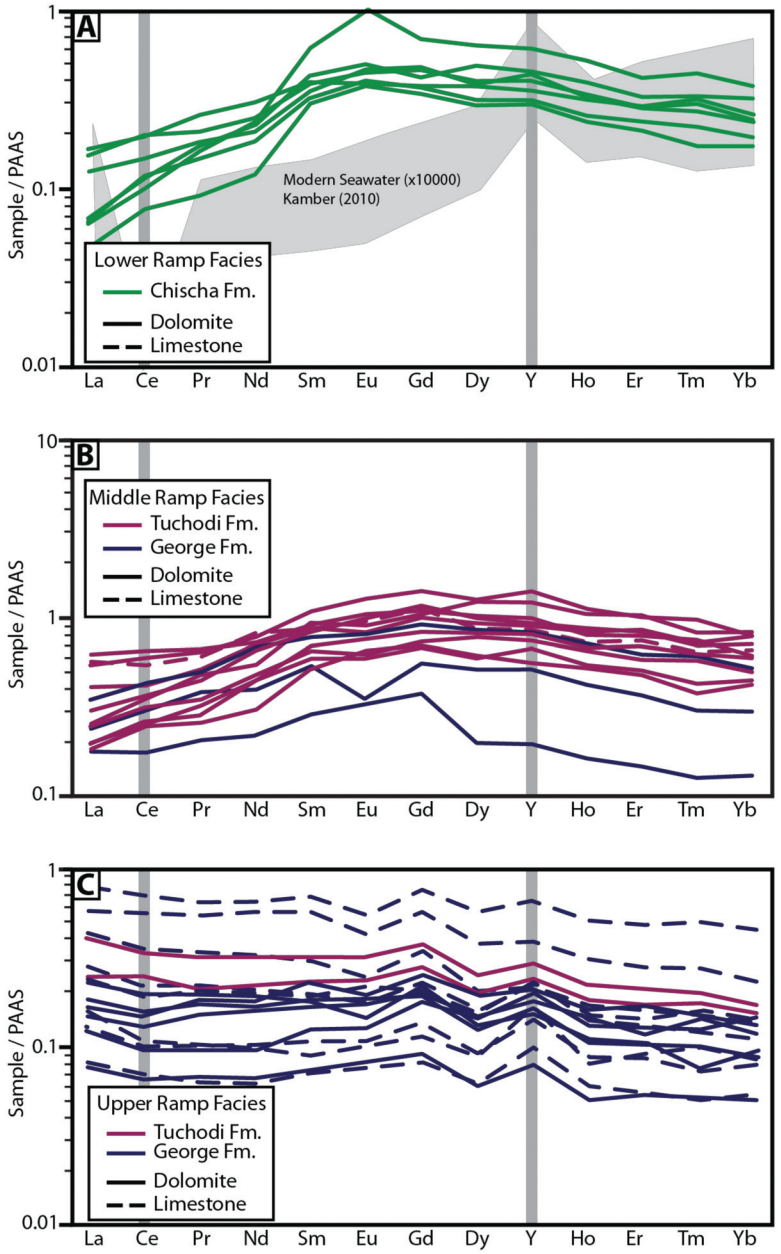

Fig. 10. REE+Y results from carbonates of the Muskwa Assemblage. Each formation and carbonate facies shows distinct REE+Y profiles. (A) Deeper lower ramp facies carbonates preserve LREE depleted profiles with no Ce anomalies. Included for comparison is the range of modern seawater REE+Y values (Kamber, 2010). (B) Mid ramp facies carbonates preserve a large LREE depletion and some positive Ce anomalies. (C) Upper ramp facies have generally flat REE+Y profiles with a negative Ce anomaly and a small LREE enrichment. All carbonate samples in ppm and normalized to PAAS (Taylor and McLennan, 1985).

had a large range of Y/Ho (27–57, this study) and variations in sample Y/Ho could just as likely be preserving prevailing water column chemistry rather than secondary detrital contamination.

Similar to Y/Ho, ΣREE+Y has been used as a detrital contamination proxy. As detrital contamination has much higher REE+Y than modern carbonates, high ΣREE+Y have been used to suggest detrital contamination (Chen and others, 2015). However, modern anoxic basins show a considerable range of ΣREE+Y concentrations between anoxic and overlying oxic waters (for example De Baar and others, 1988; Bau and others, 1997). Therefore, variations in ΣREE+Y may record variable seawater ΣREE+Y rather than contamination.

Lastly, strong MREE enrichments have been used as an indicator of alteration during diagenesis. Studies on Phanerozoic conodonts and carbonate sediments have reported that early diagenesis can drive a strong MREE enrichment (Haley and others, 2004; Kim and others, 2012). During early diagenesis, the reduction of Fe-Mn oxides and organic bound REE+Y preferentially releases MREE, which can then be incorporated into carbonate minerals (Elderfield and Sholkovitz, 1987; Haley and others, 2004; Kim and others, 2012; note that porewater REE+Y profiles should be considered relative to the overlying seawater). However, in the Proterozoic, metal cycling is likely to occur within the water column and we, therefore, cannot assume signatures of metal oxide cycling are inherited. The MREE enrichment observed in a range of Proterozoic carbonates (Frimmel, 2009; Hood and Wallace, 2014, 2015; Tang and others, 2016; Wallace and others, 2017; this study figs. 10A–10B) is more likely representative of seawater rather than porewater processes.

Thus while the development of these new tools is promising and they provide a new means to test the preservation of carbonate REE+Y, there application in the Precambrian may be limited.

A shallow water Mid-Proterozoic chemocline.—Using stratigraphic and sedimentological interpretations of the Muskwa Assemblage to place carbonate REE+Y patterns within a paleo-depth profile, there appear to be three distinct marine REE+Y patterns between upper, mid, and lower ramp carbonate facies (figs. 10 and 11). We find that the shallowest facies, the upper ramp, has a high preponderance of Ce/Ce* values normally distributed around a value of 1.0. In a marked contrast from the upper ramp, the mid-ramp facies shows two distinct Ce/Ce* populations, one normally distributed positive population ranging from 1.2 to 1.4, and a light "tail" of samples stretching from 0.79 to 1.0. The deepest facies, the lower ramp, also has two populations of Ce/Ce* values, but they have a much narrower range, with the total range of the deepest facies spanning from 0.89 to 1.14.

This systematic shift in Ce/Ce* with depth is likely best explained by comparing our results with Ce/Ce* profiles observed in modern anoxic basin chemoclines (De Baar and others, 1988; German and Elderfield, 1989; German and others, 1991; Bau and others, 1997). In modern examples (for example Cariaco Trench, Black Sea), Ce/Ce* values in surface oxic waters are near 1.0 or slightly negative and generally decrease to more negative values with depth until they reach the base of the oxic layer, where Ce/Ce* values rapidly jump to positive values as it crosses the redox boundary (De Baar and others, 1988; German and others, 1991). A number of mechanisms play a key role in this characteristic profile. At the surface ocean, REE+Y with Ce/Ce* near 1.0 is added to the water column by settling dust particles leading to a surface ocean peak in Ce concentrations (Greaves and others, 1994; Pearce and others, 2013). In oxic surface waters, Ce^{3+} is oxidized to Ce^{4+} and is preferentially scavenged from seawater by sinking particles, driving a local depletion of Ce as measured by negative Ce/Ce* values (De Baar and others, 1988; German and Elderfield, 1989; Bau and others, 1996; Bau, 1999). Ce enriched particles then settle down through the water column and reach a redox boundary where Ce is dissolved back into seawater, generating a positive Ce/Ce* anomaly at and immediately below the redox boundary. Below the redox boundary, Ce/Ce* values progressively return to values near 1.0 as

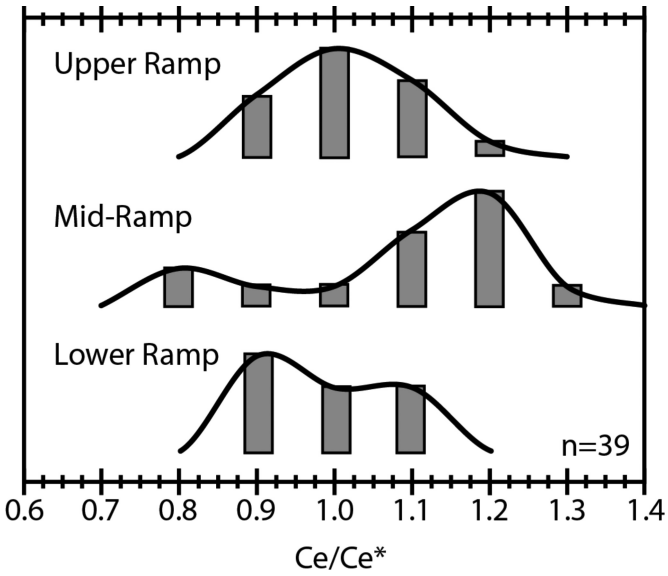

Fig. 11. A histogram of Ce/Ce* values for each carbonate facies. The upper ramp facies preserves a narrow range of Ce/Ce* values centered around 1.0. The mid-ramp facies shows two distinct Ce/Ce* populations, one normally distributed positive population ranging from 1.2–1.4, and a light "tail" of samples stretching from 0.79–1.0. The deepest facies, the lower ramp, also has two populations of Ce/Ce* values, but they have a much narrower range, with the total range of the deepest facies spanning from 0.89–1.14.

dissolved Ce-rich particles mix with Ce depleted waters rebalancing Ce values (German and Elderfield, 1989; German and others, 1991; Bau and others, 1997).

Comparing these modern examples to our Ce/Ce* results, it would appear to indicate that the Muskwa Assemblage preserved a redox chemocline within the mid-ramp facies, thus restricted to within storm-wave base and likely even within the mixed layer. The generally narrow range of Ce/Ce* values in the upper ramp environment is consistent with a shallow surface ocean setting, recording minor Ce cycling but generally low values due to surface ocean addition of dust derived Ce. The preponderance of both the most negative and positive Ce/Ce* anomalies within the mid-ramp setting is most consistent with the presence of a chemocline within this setting, where large Ce/Ce* anomalies would have formed above and below the chemocline. A return to a much narrower Ce/Ce* population in the lower-ramp likely indicates a more persistently anoxic environment below the chemocline. The lower ramp setting does contain small negative and positive Ce/Ce* populations, thus it's entirely possible that the chemocline experienced a seasonal shift in depth. Some modern anoxic basins experience similar seasonal shifts (for example Saanich inlet; German and Elderfield, 1989) due to shifts in ocean mixing rates and reductant or oxidant availability. A seasonal deepening of the chemocline during deposition of the Muskwa Assemblage would have smeared Ce/Ce* values between different paleo-environments, potentially explaining the presence of minor negative and positive Ce/Ce* values within the lower ramp facies.

Overall, these results appear most consistent with the presence of a chemocline within the mid-ramp facies of the Muskwa Assemblage, thus restricted to within storm-wave base and likely even within the mixed layer. This interpretation is consistent with prior work, which suggests that Paleo- and Mesoproterozoic oceans were largely anoxic with only a thin oxidized surface ocean (Gilleaudeau and Kah, 2015;

Reinhard and others, 2016; Tang and others, 2016; Hardisty and others, 2017; Bellefroid and others, 2018).

Understanding Muskwa Assemblage LREE depletions.—Muskwa Assemblage carbonates have a considerable range of LREE enrichments between upper- and lower-ramp settings, in addition to shifts in Ce/Ce*. However, Ce/Ce* and La/Yb, a measure of depletion, do not show a clear correlation, suggesting they do not share a similar mechanism (fig. 8A).

Neoproterozoic and Mesoproterozoic carbonates often preserve convex-upwards patterns with MREE enrichments and/or a large LREE depletion (for example Frimmel, 2009; Hood and Wallace, 2014, 2015; Wallace and others, 2017; this study). This REE+Y "MREE-bulge" and LREE depletion signature could be reflective of largely anoxic Proterozoic seawater where Fe-Mn oxide cycling occurred within the water column and in the environments of carbonate precipitation (Planavsky and others, 2011). Further, with metal oxide dissolution within the water column, other particulate matter may have taken the dominant role in REE+Y removal from seawater. In Proterozoic oceans, REE+Y patterns could have been mainly driven by sorption to organics and inorganic nano-particles (inorganic NPC), such as clays and fine-grained silicate minerals. Though there are few studies of inorganic NPC scavenging, Tepe and Bau (2016) found NPC's preferentially scavenge LREE with a small heavy REE+Y enrichment, generating dissolved REE+Y patterns similar to those observed in this study.

Regardless of what combination of processes is controlling the shape of Proterozoic REE+Y patterns, there is strong evidence that mid-Proterozoic oceans were largely anoxic with only a very shallow chemocline. Though it is difficult to precisely constrain depth, in the examined samples, the chemocline was above storm-wave base and therefore, based on modern analogies, in the upper 30 to 100 m of the surface ocean. This likely helps explain the stark contrast between Proterozoic and Phanerozoic seawater REE+Y profiles (Shields and Webb, 2004; Olivier and Boyet, 2006; Frimmel, 2009; Hood and Wallace, 2014, 2015; Wallace and others, 2017; this study). The consistency of the Mesozoic and Cenozoic REE+Y patterns is reflective of the widespread oxic oceans, whereas both less negative Ce/Ce* and more MREE enriched REE+Y profiles in Precambrian carbonates are reflective of anoxic seawater before the full-scale oxygenation of the oceans and atmosphere (for example Tang and others, 2016; Wallace and others, 2017; Bellefroid and others, 2018). Importantly, the common occurrence of weakly negative Ce/Ce* and co-occurring positive Ce/Ce* in Muskwa Assemblage carbonates and other shallow water Paleoproterozoic and Mesoproterozoic successions (Tang and others, 2016) is a clear indicator that the Mid-Proterozoic oceans were only oxygenated at the ocean surface, likely reflecting low and stable atmospheric oxygen levels. Although there are small isolated regions with a shallow chemocline in the modern oceans (for example the Chesapeake Bay; Sholkovitz and others, 1992) a very shallow water chemocline in a high-energy marine basin, is difficult to explain under a well-oxygenated atmosphere. Further, it is important to note that coeval suboxic conditions (compare with Slack and others, 2007) could have been possible even in a low pO_2 ocean if there was subduction of water masses in oligotrophic regions of the oceans.

Implications for the Mid-Proterozoic carbon cycle.—Similar to the REE+Y profile with depth, Muskwa Assemblage carbonates show a systematic decrease in $\delta^{13}C$ from shallower to deeper sedimentary facies of ~2 to 3 permil. Upper ramp facies sediments (Upper George Fm. and lower Tuchodi Fm.) have high $\delta^{13}C$ values (mean 0.49 ‰, stdev 0.57 ‰), mid-ramp facies (lower George Fm. and lower Tuchodi) have mid-range $\delta^{13}C$ values with a large variance (mean −0.59 ‰, stdev 1.10 ‰), and deeper water lower ramp (Chischa Fm. and upper Tuchodi Fm.) have more negative $\delta^{13}C$

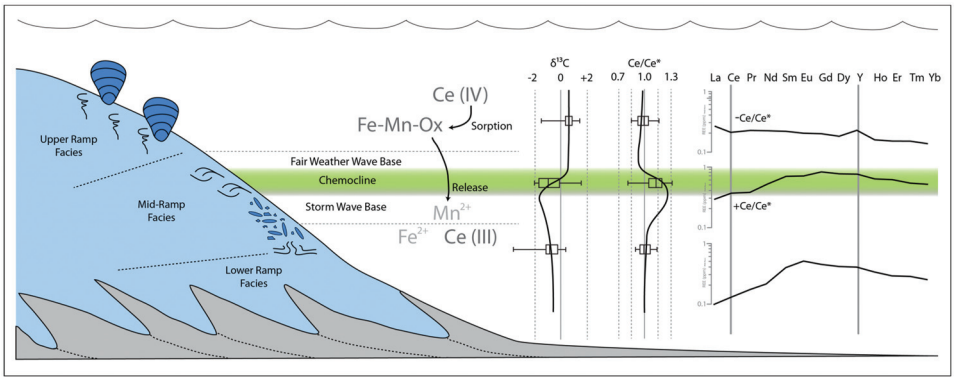

Fig. 12. A generalized interpretation of Muskwa marine chemistry. The chemocline between oxic and anoxic waters appears to form between fair weather wave-base and storm wave-base. REE+Y patterns shift across this chemocline reflected in a shift from negative to positive Ce/Ce* values (facies specific data shown in box and whiskers plot, curve represents average). Furthermore, $\delta^{13}C$ appear to also shift across the boundary, likely reflecting the oxidation of organic matter at this boundary (facies specific raw data shown as box and whisker plots, curve represents average).

values (mean −0.70 ‰, stdev 0.96 ‰). This trend is paralleled by a shift in REE+Y derived redox conditions, with a moderate but significant correlation between Ce/Ce* and $\delta^{13}C$ in upper and mid-ramp facies (R^2=0.723, fig. 8B). This correlation is not observed in deeper water facies (R^2=0.40), thus this sharp $\delta^{13}C$ gradient is likely restricted to near the chemocline where Fe-Mn cycling is most important.

Interpreting these results from a modern perspective, the ~ 2 to 3 permil $\delta^{13}C$ gradient observed in Muskwa Assemblage (fig. 8B, fig. 12) sediments is quite small. For comparison, the $\delta^{13}C$ of marine DIC across the oxic Bahama Bank shows a ~4 permil range (Patterson and Walter, 1994; Swart and Eberli, 2005), while the dominantly anoxic Black Sea shows a ~7 permil range with depth (Fry and others, 1991). As in the case of these examples, a combination of organic matter remineralization and basin restriction can lead carbonate platform or ramps to record secular changes in $\delta^{13}C$ unrelated to the global carbon cycle (Weber and Woodhead, 1969; Patterson and Walter, 1994; Holmden and others, 1998). The general consensus has been that these processes were minor in Mid-Proterozoic carbonate sequences, and high marine DIC would have muted any sharp $\delta^{13}C$ gradients (Bartley and Kah, 2004; Hotinsky and others, 2004). Consequently, this has led to the argument that any stratigraphic shift in $\delta^{13}C$ through a single Mid-Proterozoic carbonate sequence must reflect secular changes in the global carbon cycle (for example Kah and others, 2012; Gilleaudeau and Kah, 2013). Though basin restriction and organic matter oxidation are recognized to drive some form of $\delta^{13}C$ gradient, it is argued that these would only be significant across large lateral distances (Gilleaudeau and Kah, 2013). In contrast, our observation of a consistent ~ 2 to 3 ‰ $\delta^{13}C$ shift within 50 to 100m inferred paleo-depth lends some weight to the idea of steep, but small shallow water $\delta^{13}C$ gradient over a shallow chemocline during this time period.

Variability in $\delta^{13}C$ values may be linked in part to a shift in the organic matter remineralization e-folding depth (the point at which 1/e, or ~37 %, of sinking organic carbon is remineralized; Meyer and others, 2016), driving a steep $\delta^{13}C$ gradient within the water column, even if productivity was low and DIC was higher than in the modern oceans. Several authors have suggested, in a cyanobacterial dominated metazoan free world, slower export in the mid-Proterozoic could have led to more efficient organic matter remineralization and, therefore, higher $\delta^{13}C$ gradients in shallower waters

(Logan and others, 1995; Butterfield, 2011). This is debated, however, as organic matter export rates are complicated by fecal pellet disaggregation, fecal density, porosity, dust fluxes, and a number of other factors, which bring into question whether metazoan zooplankton alone could have had such a large impact and, therefore, whether there was much difference in organic matter export rates between the Mid-Proterozoic and the Neoproterozoic (for review see Planavsky and others, 2015).

The development of a $\delta^{13}C$ gradient in the Muskwa Assemblage (fig. 12) may have implications for the use of $\delta^{13}C$ as a chemostratigraphic tool. Shallow water anaerobic respiration, potentially tied to Fe-Mn cycling at the chemocline, could have driven small but significant $\delta^{13}C$ gradients in mid-Proterozoic marine DIC, similar to what is observed in Phanerozoic and modern carbonate systems (for example Fry and others, 1991; Holmden and others, 1998; LaPorte and others, 2009). Overall, we suggest that small stratigraphic shifts in $\delta^{13}C$ may not necessarily be attributed to secular global carbon cycling. Thus, caution must be used when interpreting the origins of Mid-Proterozoic carbonate $\delta^{13}C$, especially when stratigraphic context and redox conditions are unknown. Whether this feature persisted into the Neoproterozoic is unclear. Neoproterozoic carbonate stratigraphers have focused on targeting large (> 5 ‰) carbon isotope excursions for $\delta^{13}C$ chemostratigraphy (for example Halverson and others, 2005, 2010; Macdonald and others, 2010). Though their primary origins have been disputed and there are relatively few studies on $\delta^{13}C$ variations within single basins (for discussion see Swart and Eberli, 2005; Knauth and Kennedy, 2009; Derry, 2010), these excursions are largely thought to be globally synchronous (for example Rooney and others, 2015; Husson and others, 2015). Thus, Neoproterozoic $\delta^{13}C$ excursions are likely large enough to require a separate and global mechanism to explain.

CONCLUSION

The Muskwa Assemblage is a Mid-Proterozoic carbonate ramp with three distinct facies, which are developed in the lower units of the assemblage. Above fair-weather wave base, an upper ramp setting is characterized by cross-bedded sands, relatively pure carbonates (including low-relief stromatolite mounds and the development of MTS) and minor silicification. Deeper-water, lower ramp environments are dominated by rippled and laminated fine-grained dolomites and shales. A storm-wave base to fair-weather wave base facies is dominated by storm influenced marly carbonates and shows sediment reworking characteristic of a ramp setting.

REE+Y and $\delta^{13}C$ values of carbonates have depth dependent trends (fig. 12). Ce anomalies are moderately negative above fair-weather wave base but are positive between fair-weather wave base and storm-wave base. The preservation of both positive and negative Ce/Ce* indicates an active Mn cycle and a redox gradient near fair-weather wave base. Though it is unclear what the driving mechanism is for the observed MREE "bulge" REE+Y pattern in deeper waters, we suggest that this pattern is characteristic of Meso- and Neoproterozoic anoxic seawater and active water column oxide cycling.

$\delta^{13}C$ values correlate with Ce/Ce* in shallow and mid-ramp facies, and show a ~3 permil decrease with depth. This correlation suggests a small but important $\delta^{13}C$ gradient across the shallow marine chemocline. The utility of $\delta^{13}C$ as a chemostratigraphic tool must be treated with caution.

ACKNOWLEDGMENTS

The authors would like to thank M. Kunzmann and G.M. Cox for their help and support during fieldwork, as well as D.A.D. Evans for his constructive input. E.J. Bellefroid acknowledges support from the Natural Sciences and Engineering Research Council of Canada (NSERC). A.V.S.H. acknowledges support from a

NASA Astrobiology Postdoctoral Fellowship. This work was supported by the Alternative Earths NASA Astrobiology Institute. Reviews from two anonymous reviewers are gratefully acknowledged for their constructive comments.

REFERENCES CITED

Aitken, J. D., and McMechan, M. E., 1991, Middle Proterozoic Assemblages, *in* Gabrielse, H., and Yorath, C., editors, Geology of the Cordilleran Orogeny in Canada: Geological Survey of Canada, Geology of Canada, n. 4, p. 97–124.

Bailey, T. R., McArthur, J. M., Prince, H., and Thirlwall, M. F., 2000, Dissolution methods for strontium isotope stratigraphy: Whole rock analysis: Chemical Geology, v. 167, n. 3–4, p. 313–319, https://doi.org/10.1016/S0009-2541(99)00235-1

Banner, J. L., Hanson, G. N., and Meyers, W. J., 1988a, Determination of initial Sr isotopic compositions of dolostones from the Burlington-Keokuk Formation (Mississippian): Constraints from cathodoluminescence, glauconite paragenesis and analytical methods: Journal of Sedimentary Research, v. 58, n. 4, p. 673–687, https://doi.org/10.2110/jsr.58.673

——— 1988b, Rare earth element and Nd isotopic variations in regionally extensive dolomites from the Burlington-Keokuk Formation (Mississippian): Implications for REE mobility during carbonate diagenesis: Journal of Sedimentary Research, v. 58, n. 3, p. 415–432, https://doi.org/10.1306/212F8DAA-2B24-11D7-8648000102C1865D

Bartley, J. K., and Kah, L. C., 2004, Marine carbon reservoir, C_{org}-C_{carb} coupling, and the evolution of the Proterozoic carbon cycle: Geology, v. 32, n. 2, p. 129–132, https://doi.org/10.1130/G19939.1

Bau, M., 1999, Scavenging of dissolved yttrium and rare earths by precipitating iron oxyhydroxide: Experimental evidence for Ce oxidation, Y-Ho fractionation, and lanthanide tetrad effect: Geochimica et Cosmochimica Acta, v. 63, n. 1, p. 67–77, https://doi.org/10.1016/S0016-7037(99)00014-9

Bau, M., and Alexander, B., 2006, Preservation of primary REE patterns without Ce anomaly during dolomitization of Mid-Paleoproterozoic limestone and the potential re-establishment of marine anoxia immediately after the "Great Oxidation Event": South African Journal of Geology, v. 109, n. 1–2, p. 81–86, https://doi.org/10.2113/gssajg.109.1-2.81

Bau, M., and Koschinsky, A., 2009, Oxidative scavenging of cerium on hydrous Fe oxide: Evidence from the distribution of rare earth elements and yttrium between Fe oxides and Mn oxides in hydrogenetic ferromanganese crusts: Geochemical Journal, v. 43, n. 1, p. 37–47, https://doi.org/10.2343/geochemj.1.0005

Bau, M., Koschinsky, A., Dulski, P., and Hein, J. R., 1996, Comparison of the partitioning behaviours of yttrium, rare earth elements, and titanium between hydrogenetic marine ferromanganese crusts and seawater: Geochimica et Cosmochimica Acta, v. 60, n. 10, p. 1709–1725, https://doi.org/10.1016/0016-7037(96)00063-4

Bau, M., Möller, P., and Dulski, P., 1997, Yttrium and lanthanides in eastern Mediterranean seawater and their fractionation during redox-cycling: Marine Chemistry, v. 56, n. 1–2, p. 123–131, https://doi.org/10.1016/S0304-4203(96)00091-6

Bekker, A., Planavsky, N. J., Krapež, B., Rasmussen, B., Hofmann, A., Slack, J. F., Rouxel, O. J., and Konhauser, K. O., 2014, 9.18 - Iron Formations: Their Origins and Implications for Ancient Seawater Chemistry: Oxford, Elsevier, Treatise on Geochemistry (Second Edition), v. 9, p. 561–628, https://doi.org/10.1016/B978-0-08-095975-7.00719-1

Bell, R. T., ms, 1966, Precambrian rocks of the Tuchodi Lakes map-area, northeastern British Columbia: Princeton, New Jersey, Princeton University, Ph. D. thesis, 130 p.

——— 1968, Proterozoic Stratigraphy of North-Eastern British Columbia: Geological Survey of Canada Paper 67–68, 75 p., https://doi.org/10.4095/104736

Bellefroid, E. J., Hood, A. v. S., Hoffman, P. F., Thomas, M. D., Reinhard, C. T., and Planavsky, N. J., 2018, Constraints on Paleoproterozoic atmospheric oxygen levels: Proceedings of the National Academy of Sciences of the United States of America, v. 115, n. 32, p. 8104–8109, https://doi.org/10.1073/pnas.1806216115

Brasier, M. D., and Lindsay, J. F., 1998. A billion years of environmental stability and the emergence of eukaryotes: New data from northern Australia: Geology, v. 26, n. 6, p. 555–558, https://doi.org/10.1130/0091-7613(1998)026<0555:ABYOES>2.3.CO;2

Brocks, J. J., Jarrett, A. J. M., Sirantoine, E., Hallmann, C., Hoshino, Y., and Liyanage, T., 2017, The rise of algae in Cryogenian oceans and the emergence of animals: Nature, v. 548, p. 578–581, https://doi.org/10.1038/nature23457

Butterfield, N. J., 2000, Bangiomorpha pubescens n. gen., n. sp.: Implications for the evolution of sex, multicellularity, and the Mesoproterozoic/Neoproterozoic radiation of eukaryotes: Paleobiology, v. 26, n. 3, p. 386–404, https://doi.org/10.1666/0094-8373(2000)026<0386:BPNGNS>2.0.CO;2

——— 2011, Animals and the invention of the Phanerozoic Earth system: Trends in Ecology & Evolution, v. 26, n. 2, p. 81–87, https://doi.org/10.1016/j.tree.2010.11.012

Canfield, D. E., Poulton, S. W., Knoll, A. H., Narbonne, G. M., Ross, G., Goldberg, T., and Strauss, H., 2008, Ferruginous conditions dominated later Neoproterozoic deep-water chemistry: Science, v. 321, n. 5891, p. 949–952, https://doi.org/10.1126/science.1154499

Canfield, D. E., Zhang, S., Frank, A. B., Wand, X., Wang, H., Su, J., Ye, Y., and Frei, R., 2018, Highly fractionated chromium isotopes in Mesoproterozoic-aged shales and atmospheric oxygen: Nature Communications, v. 9, n. 1, article number 2871, https://doi.org/10.1038/s41467-018-05263-9

Chen, J., Algeo, T. J., Zhao, L., Chen, Z., Cao, L., Zhang, L., and Li, Y., 2015, Diagenetic uptake of rare earth

elements by bioapatite, with an example from Lower Triassic conodonts of South China: Earth-Science Reviews, v. 149, p. 181–202, https://doi.org/10.1016/j.earscirev.2015.01.013
Cole, D. B., Reinhard, C. T., Wang, X., Gueguen, B., Halverson, G. P., Gibson, T., Hodgskiss, M. S. W., McKenzie, N. R., Lyons, T. W., and Planavsky, N. J., 2016, A shale-hosted Cr isotope record of low atmospheric oxygen during the Proterozoic: Geology, v. 44, n. 7, p. 555–558, https://doi.org/10.1130/G37787.1
Colpron, M., Logan, J. M., and Mortensen, J. K., 2002, U-Pb zircon age constraint for late Neoproterozoic rifting and initiation of the lower Paleozoic passive margin of western Laurentia: Canadian Journal of Earth Sciences, v. 39, n. 2, p. 133–143, https://doi.org/10.1139/e01-069
Cook, F. A., and Van der Velden, A. J., 1993, Proterozoic crustal transition beneath the Western Canada sedimentary basin: Geology, v. 21, n. 9, p. 785–788, https://doi.org/10.1130/0091-7613(1993)021<0785:PCTBTW>2.3.CO;2
Cook, F. A., Clowes, R. M., Snyder, D. B., van der Velden, A. J., Hall, K. W., Erdmer, P., and Evenchick, C. A., 2004, Precambrian crust beneath the Mesozoic northern Canadian Cordillera discovered by Lithoprobe seismic reflection profiling: Tectonics, v. 23, n. 2, p. TC2010, https://doi.org/10.1029/2002TC001412
Crowe, S. A., Dossing, L. N., Beukes, N. J., Bau, M., Kruger, S. J., Frei, R., and Canfield, D. E., 2013, Atmospheric oxygenation three billion years ago: Nature, v. 501, p. 535–538, https://doi.org/10.1038/nature12426
D'Arcy, J., Babechuk, M. G., Døssing, L. N., Gaucher, C., and Frei, R., 2016, Processes controlling the chromium isotopic composition of river water: Constraints from basaltic river catchments: Geochimica et Cosmochimica Acta, v. 186, p. 296–315, https://doi.org/10.1016/j.gca.2016.04.027
De Baar, H. J. W., German, C. R., Elderfield, H., and van Gaans, P., 1988, Rare earth element distributions in anoxic waters of the Cariaco Trench: Geochimica et Cosmochimica Acta, v. 52, p. 1203–1219, https://doi.org/10.1016/0016-7037(88)90275-X
Derry, L. A., 2010, A burial diagenesis origin for the Ediacaran Shuram–Wonoka carbon isotope anomaly: Earth and Planetary Science Letters, v. 294, n. 1–2, p. 152–162, https://doi.org/10.1016/j.epsl.2010.03.022
Elderfield, H., and Sholkovitz, E. R., 1987, Rare earth elements in the pore waters of reducing nearshore sediments: Earth and Planetary Science Letters, v. 82, n. 3–4, p. 280–288, https://doi.org/10.1016/0012-821X(87)90202-0
Evans, D. A. D., 2003, A fundamental Precambrian–Phanerozoic shift in earth's glacial style?: Tectonophysics, v. 375, p. 353–385, https://doi.org/10.1016/S0040-1951(03)00345-7
Evans, K. V., Aleinikoff, J. N., Obradovich, J. D., and Fanning, C. M., 2000, SHRIMP U-Pb geochronology of volcanic rocks, Belt Supergroup, western Montana: Evidence for rapid deposition of sedimentary strata: Canadian Journal of Earth Sciences, v. 37, n. 9, p. 1287–1300, https://doi.org/10.1139/e00-036
Evenchick, C. A., Gabrielse, H., and Snyder, D., 2005, Crustal structure and lithology of the northern Canadian Cordillera: Alternative interpretations of SNORCLE seismic reflection lines 2a and 2b: Canadian Journal of Earth Sciences, v. 42, n. 6, p. 1149–1161, https://doi.org/10.1139/e05-009
Ferri, F., Rees, C., Nelson, J., Legun, A., Orchard, M. J., Norford, B. S., Fritz, W. H., Mortensen, J. K., and Gabites, J. E., 1999, Geology and mineral deposits of the northern Kechika Trough between Gataga River and the 60th parallel: Bulletin-British Columbia Ministry of Energy and Mines, Energy and Minerals Division, Geological Survey Branch, v. 107, p. 2.
Frimmel, H. E., 2009, Trace element distribution in Neoproterozoic carbonates as palaeoenvironmental indicator: Chemical Geology, v. 258, n. 3-4, p. 338–353, https://doi.org/10.1016/j.chemgeo.2008.10.033
Fry, B., Jannasch, H. W., Molyneaux, S. J., Wirsen, C. O., Muramoto, J. A., and King, S., 1991, Stable isotope studies of the carbon, nitrogen and sulfur cycles in the Black Sea and the Cariaco Trench: Deep Sea Research Part A. Oceanographic Research Papers, v. 38, Supplement 2, p. S1003–S1019, https://doi.org/10.1016/S0198-0149(10)80021-4
Furlanetto, F., Thorkelson, D. J., Rainbird, R. H., Davis, W. J., Gibson, H. D., and Marshall, D. D., 2016, The Paleoproterozoic Wernecke Supergroup of Yukon, Canada: Relationships to orogeny in northwestern Laurentia and basins in North America, East Australia, and China: Gondwana Research, v. 39, p. 14–40, https://doi.org/10.1016/j.gr.2016.06.007
German, C. R., and Elderfield, H., 1989, Rare earth elements in Saanich Inlet, British Columbia, a seasonally anoxic basin: Geochimica et Cosmochimica Acta, v. 53, n. 10, p. 2561–2571, https://doi.org/10.1016/0016-7037(89)90128-2
——— 1990, Application of the Ce anomaly as a paleoredox indicator: The ground rules: Paleoceanography, v. 5, n. 5, p. 823–833, https://doi.org/10.1029/PA005i005p00823
German, C. R., Holliday, B. P., and Elderfield, H., 1991, Redox cycling of rare earth elements in the suboxic zone of the Black Sea: Geochimica et Cosmochimica Acta, v. 55, n. 12, p. 3553–3558, https://doi.org/10.1016/0016-7037(91)90055-A
Gilleaudeau, G. J., and Kah, L. C., 2013, Carbon isotope records in a Mesoproterozoic epicratonic sea: Carbon cycling in a low-oxygen world: Precambrian Research, v. 228, p. 85–101, https://doi.org/10.1016/j.precamres.2013.01.006
——— 2015, Heterogeneous redox conditions and a shallow chemocline in the Mesoproterozoic ocean: Evidence from carbon–sulfur–iron relationships: Precambrian Research, v. 257, p. 94–108, https://doi.org/10.1016/j.precamres.2014.11.030
Gilleaudeau, G. J., Frei, R., Kaufman, A. J., Kah, L. C., Azmy, K., Bartley, J. K., Chernyavskiy, P., and Knoll, A. H., 2016, Oxygenation of the mid-Proterozoic atmosphere: Clues from chromium isotopes in carbonates: Geochemical Perspectives Letters, v. 2, n. 2, p. 178–187, https://doi.org/10.7185/geochemlet.1618
Greaves, M. J., Statham, P. J., and Elderfield, H., 1994, Rare earth element mobilization from marine

atmospheric dust into seawater: Marine Chemistry, v. 46, n. 3, p. 255–260, https://doi.org/10.1016/0304-4203(94)90081-7
Haley, B. A., Klinkhammer, G. P., and McManus, J., 2004, Rare earth elements in pore waters of marine sediments: Geochimica et Cosmochimica Acta, v. 68, n. 6, p. 1265–1279, https://doi.org/10.1016/j.gca.2003.09.012
Halverson, G. P., Hoffman, P. F., Schrag, D. P., Maloof, A. C., and Rice, A. H. N., 2005, Toward a Neoproterozoic composite carbon-isotope record: Geological Society of America Bulletin, v. 117, n. 9–10, p. 1181–1207, https://doi.org/10.1130/B25630.1
Halverson, G. P., Dudás, F. Ö., Maloof, A. C., and Bowring, S. A., 2007, Evolution of the $^{87}Sr/^{86}Sr$ composition of Neoproterozoic seawater: Palaeogeography, Palaeoclimatology, Palaeoecology, v. 256, n. 3–4, p. 103–129, https://doi.org/10.1016/j.palaeo.2007.02.028
Hardisty, D. S., Lu, Z., Bekker, A., Diamond, C. W., Gill, B. C., Jiang, G., Kah, L. C., Knoll, A. H., Loyd, S. J., Osburn, M. R., Planavsky, N. J., Wang, C., Zhou, X., and Lyons, T. W., 2017, Perspectives on Proterozoic surface ocean redox from iodine contents in ancient and recent carbonate: Earth and Planetary Science Letters, v. 463, p. 159–170, https://doi.org/10.1016/j.epsl.2017.01.032
Hoffman, P. F., Kaufman, A. J., Halverson, G. P., and Schrag, D. P., 1998, A Neoproterozoic Snowball Earth: Science, v. 281, n. 5381, p. 1342–1346, https://doi.org/10.1126/science.281.5381.1342
Holland, H. D., 2006, The oxygenation of the atmosphere and oceans: Philosophical Transactions of the Royal Society London B Biological Sciences, v. 361, issue 1470, p. 903–15, https://doi.org/10.1098/rstb.2006.1838
Holmden, C., Creaser, R. A., Muehlenbachs, K., Leslie, S. A., and Bergström, S. M., 1998, Isotopic evidence for geochemical decoupling between ancient epeiric seas and bordering oceans: Implications for secular curves: Geology, v. 26, n. 6, p. 567–570, https://doi.org/10.1130/0091-7613(1998)026<0567:IEFGDB>2.3.CO;2
Hood, A. v. S., and Wallace, M. W., 2014, Marine cements reveal the structure of an anoxic, ferruginous Neoproterozoic ocean: Journal of the Geological Society, v. 171, n. 6, p. 741–744, https://doi.org/10.1144/jgs2013-099
——— 2015, Extreme ocean anoxia during the Late Cryogenian recorded in reefal carbonates of Southern Australia: Precambrian Research, v. 261, p. 96–111, https://doi.org/10.1016/j.precamres.2015.02.008
Hood, A. v. S., Planavsky, N. J., Wallace, M. W., and Wang, X., 2018, The Effects of Diagenesis on Geochemical Paleoredox Proxies in Sedimentary Carbonates: Geochimica et Cosmochimica Acta, v. 232, p. 265–287, https://doi.org/10.1016/j.gca.2018.04.022
Hotinski, R. M., Kump, L. R., and Arthur, M. A., 2004, The effectiveness of the Paleoproterozoic biological pump: A $\delta^{13}C$ gradient from platform carbonates of the Pethei Group (Great Slave Lake Supergroup, NWT): Geological Society of America Bulletin, v. 116, n. 5–6, p. 539–554, https://doi.org/10.1130/B25272.1
Husson, J. M., Maloof, A. C., Schoene, B., Chen, C. Y., and Higgins, J. A., 2015, Stratigraphic expression of Earth's deepest $\delta^{13}C$ excursion in the Wonoka Formation of South Australia: American Journal of Science, v. 315, n. 1, p. 1–45, https://doi.org/10.2475/01.2015.01
James, N. P., Narbonne, G. M., and Sherman, A. G., 1998, Molar-tooth carbonates: Shallow subtidal facies of the Mid-to Late Proterozoic: Journal of Sedimentary Research, v. 68, n. 5, p. 716–722, https://doi.org/10.2110/jsr.68.716
Kah, L. C., Sherman, A. G., Narbonne, G. M., Knoll, A. H., and Kaufman, A. J., 1999, $\delta^{13}C$ stratigraphy of the Proterozoic Bylot Supergroup, Baffin Island, Canada: Implications for regional lithostratigraphic correlations: Canadian Journal of Earth Sciences, v. 36, n. 3, p. 313–332, https://doi.org/10.1139/e98-100
Kah, L. C., Bartley, J. K., and Teal, D. A., 2012, Chemostratigraphy of the Late Mesoproterozoic Atar Group, Taoudeni Basin, Mauritania: Muted isotopic variability, facies correlation, and global isotopic trends: Precambrian Research, v. 200–203, p. 82–103, https://doi.org/10.1016/j.precamres.2012.01.011
Kamber, B., 2010, Archean mafic–ultramafic volcanic landmasses and their effect on ocean–atmosphere chemistry: Chemical Geology, v. 274, n. 1–2, p. 19–28, https://doi.org/10.1016/j.chemgeo.2010.03.009
Kamber, B. S., and Webb, G. E., 2001, The geochemistry of late Archaean microbial carbonate: Implications for ocean chemistry and continental erosion history: Geochimica et Cosmochimica Acta, v. 65, n. 15, p. 2509–2525, https://doi.org/10.1016/S0016-7037(01)00613-5
Kamber, B. S., Greig, A., and Collerson, K. D., 2005, A new estimate for the composition of weathered young upper continental crust from alluvial sediments, Queensland, Australia: Geochimica et Cosmochimica Acta, v. 69, n. 4, p. 1041–1058, https://doi.org/10.1016/j.gca.2004.08.020
Kenward, P. A., Goldstein, R. H., González, L. A., and Roberts, J. A., 2009, Precipitation of low-temperature dolomite from an anaerobic microbial consortium: The role of methanogenic Archaea: Geobiology, v. 7, n. 5, p. 556–565, https://doi.org/10.1111/j.1472-4669.2009.00210.x
Kim, J., Torres, M. E., Haley, B. A., Kastner, M., Pohlman, J. W., Riedel, M., and Lee, Y., 2012, The effect of diagenesis and fluid migration on rare earth element distribution in pore fluids of the northern Cascadia accretionary margin: Chemical Geology, v. 291, p. 152–165, https://doi.org/10.1016/j.chemgeo.2011.10.010
Knauth, L. P., and Kennedy, M. J., 2009, The late Precambrian greening of the Earth: Nature, v. 460, p. 728–732, https://doi.org/10.1038/nature08213
Knoll, A. H., 2014, Paleobiological Perspectives on Early Eukaryotic Evolution: Cold Spring Harbor Perspectives in Biology, v. 6, https://doi.org/10.1101/cshperspect.a016121
Kump, L. R., 2008, The rise of atmospheric oxygen: Nature, v. 451, p. 277–278, https://doi.org/10.1038/nature06587
Lamb, D. M., Awramik, S. M., Chapman, D. J., and Zhu, S., 2009, Evidence for eukaryotic diversification in

the ~1800 million-year-old Changzhougou Formation, North China: Precambrian Research, v. 173, n. 1–4, p. 93–104, https://doi.org/10.1016/j.precamres.2009.05.005
LaPorte, D. F., Holmden, C., Patterson, W. P., Loxton, J. D., Melchin, M. J., Mitchell, C. E., Finney, S. C., and Sheets, H. D., 2009, Local and global perspectives on carbon and nitrogen cycling during the Hirnantian glaciation: Palaeogeography, Palaeoclimatology, Palaeoecology, v. 276, n. 1–4, p. 182–195, https://doi.org/10.1016/j.palaeo.2009.03.009
Lawrence, M. G., Greig, A., Collerson, K. D., and Kamber, B. S., 2006, Rare Earth Element and Yttrium Variability in South East Queensland Waterways: Aquatic Geochemistry, v. 12, n. 1, p. 39–72, https://doi.org/10.1007/s10498-005-4471-8
LeCheminant, A. N., and Heaman, L. M., 1994, 779 Ma mafic magmatism in northwest Canadian Shield and Northern Cordilerra: A new regional time marker: Berkeley, California, Eighth International Conference on Geochronology, Cosmochronology and Isotope Geology, U.S. Geological Survey Circular 1107, p. 197.
Liu, C., Wang, Z., and Raub, T. D., 2013, Geochemical constraints on the origin of Marinoan cap dolostones from Nuccaleena Formation, South Australia: Chemical Geology, v. 351, p. 95–104, https://doi.org/10.1016/j.chemgeo.2013.05.012
Liu, X. M., Hardisty, D., Lyons, T. W., and Swart, P. K., 2019, Evaluating the fidelity of the cerium paleoredox tracer during variable carbonate diagenesis on the Great Bahamas Bank: Geochimica et Cosmochimica Acta, v. 248, p. 25–42, https://doi.org/10.1016/j.gca.2018.12.028
Liu, Y. G., and Schmitt, R. A., 1984, Chemical profiles in sediment and basalt samples from deep-sea drilling project Leg 74, Hole 525A, Walvis Ridge: Initial Reports of the Deep Sea Drilling Project, v. 74, p. 713–730, https://doi.org/10.2973/dsdp.proc.74.123.1984
Logan, G. A., Hayes, J. M., Hieshima, G. B., and Summons, R. E., 1995, Terminal Proterozoic reorganization of biogeochemical cycles: Nature, v. 376, p. 53–56, https://doi.org/10.1038/376053a0
Long, D. G. F., Devaney, J. R., and Pratt, B. R., 1999, Tectonostratigraphic framework of the Mesoproterozoic Muskwa assemblage, northern British Columbia: Proceedings of the Slave–northern Cordilleran lithospheric evolution (SNORCLE) transect and Cordilleran tectonics workshop meeting, March 5–7, University of Calgary, Calgary, Alberta, Canada, p. 5–7.
Lyons, T. W., Reinhard, C. T., and Planavsky, N. J., 2014, The rise of oxygen in Earth/'s early ocean and atmosphere: Nature, v. 506, p. 307–315, https://doi.org/10.1038/nature13068
Macdonald, F. A., Schmitz, M. D., Crowley, J. L., Roots, C. F., Jones, D. S., Maloof, A. C., Strauss, J. V., Cohen, P. A., Johnston, D. T., and Schrag, D. P., 2010, Calibrating the Cryogenian: Science, v. 327, n. 5970, p. 1241–1243, https://doi.org/10.1126/science.1183325
Maliva, R. G., Knoll, A. H., and Simonson, B. M., 2005, Secular change in the Precambrian silica cycle: Insights from chert petrology: GSA Bulletin, v. 117, n. 7–8, p. 835–845, https://doi.org/10.1130/B25555.1
Meyer, K. M., Ridgwell, A., and Payne, J. L., 2016, The influence of the biological pump on ocean chemistry: Implications for long-term trends in marine redox chemistry, the global carbon cycle, and marine animal ecosystems: Geobiology, v. 14, n. 3, p. 207–219, https://doi.org/10.1111/gbi.12176
Mitchell, R. L., and Sheldon, N. D., 2009, Weathering and paleosol formation in the 1.1 Ga Keweenawan Rift: Precambrian Research, v. 168, n. 3–4, p. 271–283, https://doi.org/10.1016/j.precamres.2008.09.013
Nothdurft, L. D., Webb, G. E., and Kamber, B. S., 2004, Rare earth element geochemistry of Late Devonian reefal carbonates, Canning Basin, Western Australia: Confirmation of a seawater REE proxy in ancient limestones: Geochimica et Cosmochimica Acta, v. 68, n. 2, p. 263–283, https://doi.org/10.1016/S0016-7037(03)00422-8
O'Connor, M. P., 1972, Classification and environmental interpretation of the cryptalgal organosedimentary "molar-tooth" structure from the Late Precambrian Belt-Purcell Supergroup: The Journal of Geology, v. 80, n. 5, p. 592–610, https://doi.org/10.1086/627783
Olivier, N., and Boyet, M., 2006, Rare earth and trace elements of microbialites in Upper Jurassic coral- and sponge-microbialite reefs: Chemical Geology, v. 230, n. 1–2, p. 105–123, https://doi.org/10.1016/j.chemgeo.2005.12.002
Olson, S. L., Kump, L. R., and Kasting, J. F., 2013, Quantifying the areal extent and dissolved oxygen concentrations of Archean oxygen oases: Chemical Geology, v. 362, p. 35–43, https://doi.org/10.1016/j.chemgeo.2013.08.012
Patterson, W. P., and Walter, L. M., 1994, Depletion of ^{13}C in seawater ΣCO_2 on modern carbonate platforms: Significance for the carbon isotopic record of carbonates: Geology, v. 22, p. 885–888, https://doi.org/10.1130/0091-7613(1994)022<0885:DOCISC>2.3.CO;2
Pearce, C. R., Jones, M. T., Oelkers, E. H., Pradoux, C., and Jeandel, C., 2013, The effect of particulate dissolution on the neodymium (Nd) isotope and Rare Earth Element (REE) composition of seawater: Earth and Planetary Science Letters, v. 369–370, p. 138–147, https://doi.org/10.1016/j.epsl.2013.03.023
Peng, Y. B., Bao, H. M., and Yuan, X. L., 2009, New morphological observations for Paleoproterozoic acritarchs from the Chuanlinggou Formation, North China: Precambrian Research, v. 168, n. 3–4, p. 223–232, https://doi.org/10.1016/j.precamres.2008.10.005
Pinto, J. P., and Holland, H. D., 1988, Paleosols and the evolution of the atmosphere; Part II, *in* Reinhardt, J., and Sigleo, W. R., editors, Paleosols and Weathering Through Geologic Time: Principles and Applications: Geological Society of America Special Papers, v. 216, https://doi.org/10.1130/SPE216-p21
Planavsky, N., Bekker, A., Rouxel, O. J., Kamber, B., Hofmann, A., Knudsen, A., and Lyons, T. W., 2010, Rare Earth Element and yttrium compositions of Archean and Paleoproterozoic Fe formations revisited: New perspectives on the significance and mechanisms of deposition: Geochimica et Cosmochimica Acta, v. 74, n. 22, p. 6387–6405, https://doi.org/10.1016/j.gca.2010.07.021
Planavsky, N. J., McGoldrick, P., Scott, C. T., Li, C., Reinhard, C. T., Kelly, A. E., Chu, X. L., Bekker, A., Love,

G. D., and Lyons, T. W., 2011, Widespread iron-rich conditions in the mid-Proterozoic ocean: Nature, v. 477, p. 448–451, https://doi.org/10.1038/nature10327

Planavsky, N. J., Reinhard, C. T., Wang, X., Thomson, D., McGoldrick, P., Rainbird, R. H., Johnson, T., Fischer, W. W., and Lyons, T. W., 2014, Low Mid-Proterozoic atmospheric oxygen levels and the delayed rise of animals: Science, v. 346, n. 6209, p. 635–638, https://doi.org/10.1126/science.1258410

Planavsky, N. J., Tarhan, L. G., Bellefroid, E. J., Evans, D. A. D., Reinhard, C. T., Love, G. D., and Lyons, T. W., 2015, Late Proterozoic transitions in climate, oxygen, and tectonics, and the rise of complex life, *in* Polly, P. D., Head, J. J., and Fox, D. L., editors, Earth-life transitions: Paleobiology in the context of earth system evolution: Boulder, Colorado, Paleontological Society Papers, v. 21, p. 47–82.

Poulton, S. W., and Canfield, D. E., 2011, Ferruginous conditions: A dominant feature of the ocean through Earth's history: Elements, v. 7, n. 2, p. 107–112, https://doi.org/10.2113/gselements.7.2.107

Pourmand, A., Dauphas, N., and Ireland, T. J., 2012, A novel extraction chromatography and MC-ICP-MS technique for rapid analysis of REE, Sc and Y: Revising CI-chondrite and Post-Archean Australian Shale (PAAS) abundances: Chemical Geology, v. 291, p. 38–54, https://doi.org/10.1016/j.chemgeo.2011.08.011

Rainbird, R. H., Stern, R. A., Rayner, N., and Jefferson, C. W., 2007, Age, provenance, and regional correlation of the Athabasca Group, Saskatchewan and Alberta, constrained by igneous and detrital zircon geochronology: Bulletin-Geological Survey of Canada, v. 588, p. 193, https://doi.org/10.4095/223761

Reinhard, C. T., Planavsky, N. J., Olson, S. L., Lyons, T. W., and Erwin, D. H., 2016, Earth's oxygen cycle and the evolution of animal life: Proceedings of the National Academy of Sciences, v. 113, n. 32, p. 8933–8938, https://doi.org/10.1073/pnas.1521544113

Rooney, A. D., Strauss, J. V., Brandon, A. D., and Macdonald, F. A., 2015, A Cryogenian chronology: Two long-lasting synchronous Neoproterozoic glaciations: Geology, v. 43, p. 459–462, https://doi.org/10.1130/G36511.1

Ross, G. M., and Villeneuve, M., 2003, Provenance of the Mesoproterozoic (1.45 Ga) Belt basin (western North America): Another piece in the pre-Rodinia paleogeographic puzzle: Geological Society of America Bulletin, v. 115, n. 10, p. 1191–1217, https://doi.org/10.1130/B25209.1

Ross, G. M., Villeneuve, M. E., and Theriault, R. J., 2001, Isotopic provenance of the lower Muskwa assemblage (Mesoproterozoic, Rocky Mountains, British Columbia): New clues to correlation and source areas: Precambrian Research, v. 111, n. 1–4, p. 57–77, https://doi.org/10.1016/S0301-9268(01)00156-5

Satkoski, A. M., Lowe, D. R., Beard, B. L., Coleman, M. L., and Johnson, C. M., 2016, A high continental weathering flux into Paleoarchean seawater revealed by strontium isotope analysis of 3.26 Ga barite: Earth and Planetary Science Letters, v. 454, p. 28–35, https://doi.org/10.1016/j.epsl.2016.08.032

Shaw, H. F., and Wasserburg, G. J., 1985, Sm-Nd in marine carbonates and phosphates: Implications for Nd isotopes in seawater and crustal ages: Geochimica et Cosmochimica Acta, v. 49, n. 2, p. 503–518, https://doi.org/10.1016/0016-7037(85)90042-0

Shields, G. A., 2002, 'Molar-tooth microspar': A chemical explanation for its disappearance ~ 750 Ma: Terra Nova, v. 14, n. 2, p. 108–113, https://doi.org/10.1046/j.1365-3121.2002.00396.x

Shields, G. A., and Veizer, J., 2002, Precambrian marine carbonate isotope database: Version 1.1: Geochemistry, Geophysics, Geosystems, v. 3, n. 6, p. 1 of 12–12 of 12, https://doi.org/10.1029/2001GC000266

Shields, G. A., and Webb, G. E., 2004, Has the REE composition of seawater changed over geological time?: Chemical Geology, v. 204, n. 1–2, p. 103–107, https://doi.org/10.1016/j.chemgeo.2003.09.010

Sholkovitz, E. R., and Shen, G. T., 1995, The incorporation of rare earth elements in modern coral: Geochimica et Cosmochimica Acta, v. 59, n. 13, p. 2749–2756, https://doi.org/10.1016/0016-7037(95)00170-5

Sholkovitz, E. R., Shaw, T. J., and Schneider, D. L., 1992, The geochemistry of rare earth elements in the seasonally anoxic water column and porewaters of Chesapeake Bay: Geochimica et Cosmochimica Acta, v. 56, n. 9, p. 3389–3402, https://doi.org/10.1016/0016-7037(92)90386-W

Slack, J. F., Grenne, T., Bekker, A., Rouxel, O. J., and Lindberg, P. A., 2007, Suboxic deep seawater in the late Paleoproterozoic: Evidence from hematitic chert and iron formation related to seafloor-hydrothermal sulfide deposits, central Arizona, USA: Earth and Planetary Science Letters, v. 255, n. 1–2, p. 243–256, https://doi.org/10.1016/j.epsl.2006.12.018

Smith, A. G., 2016, A review of molar-tooth structures with some speculations on their origin: Geological Society of America Special Papers, v. 522, https://doi.org/10.1130/2016.2522(03)

Sperling, E. A., Rooney, A. D., Hays, L., Sergeev, V. N., Vorob'eva, N. G., Sergeeva, N. D., Selby, D., Johnston, D. T., and Knoll, A. H., 2014, Redox heterogeneity of subsurface waters in the Mesoproterozoic ocean: Geobiology, v. 12, n. 5, p. 373–386, https://doi.org/10.1111/gbi.12091

Swart, P. K., and Eberli, G., 2005, The nature of the $\delta^{13}C$ of periplatform sediments: Implications for stratigraphy and the global carbon cycle: Sedimentary Geology, v. 175, n. 1–4, p. 115–129, https://doi.org/10.1016/j.sedgeo.2004.12.029

Tang, D., Shi, X., Wang, X., and Jiang, G., 2016, Extremely low oxygen concentration in mid-Proterozoic shallow seawaters: Precambrian Research, v. 276, p. 145–157, https://doi.org/10.1016/j.precamres.2016.02.005

Taylor, G. C., and Stott, D. F., 1973, Tuchodi Lakes map-area, British Columbia: Geological Survey of Canada, Memoir 373.

Taylor, S. R., and McLennan, S. M., 1985, The continental crust: its composition and evolution: London, United Kingdom, Blackwell, 312 p.

Tepe, N., and Bau, M., 2016, Behavior of rare earth elements and yttrium during simulation of arctic estuarine mixing between glacial-fed river waters and seawater and the impact of inorganic (nano-) particles: Chemical Geology, v. 438, p. 134–145, https://doi.org/10.1016/j.chemgeo.2016.06.001

Thompson, R. I., 1981, The nature and significance of large 'blind' thrusts within the northern Rocky Mountains of Canada: Geological Society, London, Special Publications, v. 9, p. 449–462, https://doi.org/10.1144/GSL.SP.1981.009.01.40

Tosca, N. J., Johnston, D. T., Mushegian, A., Rothman, D. H., Summons, R. E., and Knoll, A. H., 2010, Clay mineralogy, organic carbon burial, and redox evolution in Proterozoic oceans: Geochimica et Cosmochimica Acta, v. 74, n. 5, p. 1579–1592, https://doi.org/10.1016/j.gca.2009.12.001

Tostevin, R., Shields, G. A., Tarbuck, G. M., He, T., Clarkson, M. O., and Wood, R. A., 2016, Effective use of cerium anomalies as a redox proxy in carbonate-dominated marine settings: Chemical Geology, v. 438, p. 146–162, https://doi.org/10.1016/j.chemgeo.2016.06.027

Tucker, M. E., 1983, Diagenesis, geochemistry, and origin of a Precambrian dolomite: The Beck Spring Dolomite of eastern California: Journal of Sedimentary Research, v. 53, n. 4, p. 1097–1119, https://doi.org/10.1306/212F8323-2B24-11D7-8648000102C1865D

Villeneuve, M. E., Thériault, R. J., and Ross, G. M., 1991, U–Pb ages and Sm–Nd signature of two subsurface granites from the Fort Simpson magnetic high, northwest Canada: Canadian Journal of Earth Sciences, v. 28, n. 7, p. 1003–1008, https://doi.org/10.1139/e91-091

Wacey, D., Wright, D. T., and Boyce, A. J., 2007, A stable isotope study of microbial dolomite formation in the Coorong Region, South Australia: Chemical Geology, v. 244, n. 1–2, p. 155–174, https://doi.org/10.1016/j.chemgeo.2007.06.032

Wallace, M. W., Hood, A. v. S., Shuster, A., Greig, A., Planavsky, N. J., and Reed, C. P., 2017, Oxygenation history of the Neoproterozoic to early Phanerozoic and the rise of land plants: Earth and Planetary Science Letters, v. 466, p. 12–19, https://doi.org/10.1016/j.epsl.2017.02.046

Wang, X., Johnson, T. M., and Ellis, A. S., 2015, Equilibrium isotopic fractionation and isotopic exchange kinetics between Cr(III) and Cr(VI): Geochimica et Cosmochimica Acta, v. 153, p. 72–90, https://doi.org/10.1016/j.gca.2015.01.003

Weber, J. N., and Woodhead, P. M. J., 1969, Factors affecting the carbon and oxygen isotopic composition of marine carbonate sediments—II. Heron Island, Great Barrier Reef, Australia: Geochimica et Cosmochimica Acta, v. 33, n. 1, p. 19–38, https://doi.org/10.1016/0016-7037(69)90090-8

Wood, R. A., Poulton, S. W., Prave, A. R., Hoffmann, K. H., Clarkson, M. O., Guilbaud, R., Lyne, J. W., Tostevin, R., Bowyer, F., Penny, A. M., Curtis, A., and Kasemann, S. A., 2015, Dynamic redox conditions control late Ediacaran metazoan ecosystems in the Nama Group, Namibia: Precambrian Research, v. 261, p. 252–271, https://doi.org/10.1016/j.precamres.2015.02.004

Zhao, L., Chen, Z., Algeo, T. J., Chen, J., Chen, Y., Tong, J., Gao, S., Zhou, L., Hu, Z., and Liu, Y., 2013, Rare-earth element patterns in conodont albid crowns: Evidence for massive inputs of volcanic ash during the latest Permian biocrisis?: Global and Planetary Change, v. 105, p. 135–151, https://doi.org/10.1016/j.gloplacha.2012.09.001

Zhao, M., and Zheng, Y., 2017, A geochemical framework for retrieving the linked depositional and diagenetic histories of marine carbonates: Earth and Planetary Science Letters, v. 460, p. 213–221, https://doi.org/10.1016/j.epsl.2016.11.033

Zhong, S., and Mucci, A., 1995, Partitioning of rare earth elements (REEs) between calcite and seawater solutions at 25 °C and 1 atm, and high dissolved REE concentrations: Geochimica et Cosmochimica Acta, v. 59, n. 3, p. 443–453, https://doi.org/10.1016/0016-7037(94)00381-U